Pellets/block bentonite barriers: laboratory study of their evolution upon hydration

María Victoria Villar[a], Rubén Javier Iglesias, Carlos Gutiérrez-Álvarez, Beatriz Carbonell

Centro de Investigaciones Energéticas, Medioambientales y Tecnológicas (CIEMAT), Avd. Complutense 40, 28040 Madrid, Spain

[a]corresponding author: mv.villar@ciemat.es, +34 913466391

1 Introduction

The backfilling and sealing of deposition galleries or holes and access galleries and shafts is an important part of the nuclear waste underground repository design. Openings created during the construction of the repository are potential preferential pathways for water, gas and radionuclides migration, and have to be effectively sealed. Bentonite or bentonite-based mixtures have been proposed as backfill and sealing materials for their low permeability, high swelling capacity and high retention capacity. To enhance these properties bentonite has to be compacted, and dry density values of between 1.45 and 1.65 g/cm^3 are usually considered appropriate to ensure the main safety functions of the clay barrier (Sellin and Leupin 2013). The design of clay barriers has been mainly based on using blocks of compacted bentonite and for this reason these materials have been widely

characterised in the form of high-density pre-compacted blocks, which have also been used in large-scale experiments (e.g. Dixon et al. 2002, ENRESA 2006, SKB 2010).

The use of high-density bentonite pellets (combined or not with powdered bentonite) as barrier material was also proposed several decades ago (Salo & Kukkola 1989, Volckaert et al. 1996). The manufacturing of high-density pellets usually involves the pre-heating of bentonite powder so that a drier and more compressible material can be produced and compacted. The advantage of this material is that it is easy to manufacture and install: the bentonite pellets can be emplaced using auger discharge tubes or even pneumatic projection techniques. Thus, the backfilling operation becomes an easier and potentially robotised procedure. The initial works using pellets considered vertical emplacement of the canister. This was the case of the large-scale demonstration experiment RESEAL, where a mixture of high-density bentonite pellets and bentonite powder was used to backfill a vertical shaft at the Hades Underground Research Facility in Mol, Belgium (Volckaert et al. 2000, van Geet et al. 2009). The pellets used in that project were all manufactured in the same size and shape from FoCa bentonite, and the effect of the pellet/powder ratio on the mixture properties was also tested in the laboratory (e.g. Imbert et al. 2002). More recently, the Institut de Radioprotection et de Sûreté Nucléaire (IRSN, France) studied the use of MX-80 bentonite pellets/powder mixtures as backfill material, including both laboratory (Molinero Guerra 2018) and in situ investigations performed at the Tournemire Underground Research Laboratory (URL, France, https://www.irsn.fr/dechets/recherche/programmes/scellement-stockage/Pages/essais-in-situ.aspx), whereas the Full-Scale Seal test (FSS), run by the French nuclear waste agency (ANDRA), tested this kind of mixtures in a surface facility as a seal for repository concepts both for high and intermediate-level radioactive wastes (Bosgiraud and Foin 2016). The use of regular pellets combined with powder is currently being tested in the framework of the VSEAL project to backfill vertical shafts at the Tournemire facility (e.g. Alcantara et al. 2020).

However, in the case of horizontal placement, a rigid support for the canister is needed, what can be achieved by the combined use of a lower bed made of highly compacted bentonite blocks in which the waste canister rests and an upper buffer made of granular bentonite material (GBM, i.e. pellets). This disposal concept has been adopted by the Swiss waste management agency, and is described in detail in NAGRA (2019) and references therein. The pellets/blocks construction concept was initially demonstrated in the large-scale Engineered Barrier Emplacement Experiment (EB), carried out at the Mont Terri URL, which is excavated in Opalinus Clay, using FEBEX bentonite to construct the two-component barrier (ENRESA 2005, García-Siñeriz et al. 2015). Afterwards, other large-scale experiments have been launched at the Mont Terri URL (e.g. HE-E and FE, using MX-80 bentonite) to investigate the performance of this type of material under actual operational conditions (Gaus et al. 2014, Müller et al. 2017). In all the projects mentioned in this paragraph, the bentonite pellets had irregular shapes and different sizes (15-0.4 mm), and they were combined in granulometric curves optimized to give as high as possible overall dry densities avoiding at the same time excessive segregation.

The blocks used to support the containers will be manufactured from the bentonite with hygroscopic water content (or higher than hygroscopic in some disposal concepts) compacted at a high dry density. In contrast, the initial water content of the pellets will be low (because of the drying process prior to manufacturing), and they will be poured by auger conveyors or projected. As a result, the density of the GBM once emplaced will be much lower than that of the compacted blocks. Furthermore, the two materials will also be very different in terms of their pore size distribution, with larger pores expected in the GBM part (e.g. Hoffmann et al. 2007). Hence, it is clear that the combined use of pellets and blocks in the same section of the barrier introduces difficulties in the understanding and modelling of the system performance that have to be addressed. So far there is just a large-scale in situ test with a two-component barrier already dismantled (the EB test at Mont Terri mentioned above). The more relevant observation obtained in the dismantling of the test was

the considerable homogenization of the dry density of blocks and pellets along a vertical section, although differences in dry density persisted, with the blocks still having overall higher dry density than the GBM (García-Siñeriz et al. 2015, Gens et al. 2021).

In this context, the overall objective of the BEACON (Bentonite Mechanical Evolution) project was to evaluate the consequences of heterogeneities on the performance of bentonite barriers in geological repositories for high-level radioactive waste. Although the bentonite buffer shows a natural tendency towards homogenisation, long-term observations both in large-scale and in laboratory tests revealed that a degree of heterogeneity may persist (e.g. Villar et al. 2020, Bernachy-Barbe et al. 2020). In this respect, CIEMAT carried out in the framework of this project a series of tests in cells to evaluate one of the sources of bentonite heterogeneity: the combination in the same barrier of pellets and blocks of compacted bentonite, whose initial dry densities and structures noticeably differ. The aim of this investigation was to obtain qualitative and quantitative information about the evolution, at laboratory scale, of initially inhomogeneous bentonite samples (pellets/blocks) upon hydration under isothermal conditions. Both in the laboratory and in the real case, this evolution might be affected by the characteristics of the barrier system (the particular dry density and water content of each barrier component as well as their sizes) and by the boundary conditions, such as the existence of gaps, temperature and water salinity and availability. In the present research two factors potentially affecting the mechanical evolution of a two-component barrier were analysed: water availability and barrier configuration. Thus, the tests were performed either under constant pressure conditions, simulating a repository excavated in crystalline host rock with plenty of water, such as the underground laboratory of Grimsel (https://www.grimsel.com/), or under low water inflow rate, simulating a repository with scarce water availability, which would be the case of clay host rocks (Grambow 2016), such as the underground laboratory in Mont Terri (https://www.mont-terri.ch/). An additional variable analysed in this work was the influence of hydrating through the pellets or the block part.

To date no tests analysing the hydro-mechanical behaviour of two-component bentonite samples in the laboratory have been published, although Martikainen et al. (2018) performed two similar tests in terms of geometry that were briefly reported and modeled by several groups in Talandier (2019) and Abed and Solowski (2019). Smaller oedometric tests (height 5 cm, diameter 6 cm) in which the two components were blocks of different dry density or pellets and powder were performed by the French Alternative Energies and Atomic Energy Commission (CEA) in the context of the Beacon project (Baryla et al., 2019, Bernachy-Barbe, 2021). Exercises performed to model tests involving saturation of two-component barriers highlighted the fact that the partition between micro and macro porosity was different for the two bentonite materials (Talandier 2019). The conclusion was that double porosity models appear very suitable to simulate the mechanical behaviour of bentonite compacted blocks, bentonite pellets and their combination in a single section of the engineered barrier. More recently, triple porosity models considering inter-pellet pore space, void space between clay aggregates inside pellets and space inside aggregates, have been proposed to model the hydro-mechanical behaviour of pellets/powder mixtures (Navarro et al. 2020).

2 Material and methods

Isochoric infiltration tests were performed in two-component samples, half of them consisting of a bentonite compacted block and the other half of a pellet mixture. Two types of cells were used: a large-scale oedometer (MGR) and a transparent cell (CW). In most tests the lower half of the cell was filled with bentonite pellets with an average dry density close to 1.30 g/cm^3 and the upper part by a 1.60 g/cm^3 bentonite block (in two tests the placement was in reverse). In all cases hydration with deionised water took place through the bottom at ambient temperature. These kinds of tests were complementary: whereas MGR tests provided quantitative data, the information provided by the CW test was mostly visual and qualitative.

2.1 Material

The material used in the laboratory tests was a bentonite extracted from the Cortijo de Archidona quarry (Almería, Spain) at two different moments. The first batch, known as FEBEX bentonite, was extracted in 1995 and is a granulate used to obtain the compacted blocks. The second batch was extracted in 2001 and was used to manufacture the pellets.

The FEBEX bentonite is a 900-t batch of bentonite processed in 1996 for the FEBEX project. The processing consisted in homogenisation, air-drying and manual removing of volcanic pebbles on site and, at the factory, crumbling, drying in a rotary oven at temperatures between 50 and 60°C to a water content of around 13%, and sieving through a 5-mm mesh. The physico-chemical properties of the FEBEX bentonite, as well as its most relevant thermo-hydro-mechanical and geochemical characteristics were reported in ENRESA (2006) and updated in e.g. Villar (2017).

The smectite content of the FEBEX bentonite is close to 90 wt.%. The smectitic phases are actually made up of a montmorillonite-illite mixed layer, with 10-15 wt.% of illite layers. Besides, the bentonite contains variable quantities of quartz, plagioclase, K-felspar, calcite, and cristobalite-trydimite. The cation exchange capacity is 98±2 meq/100g, the main exchangeable cations being calcium (35±2 meq/100g), magnesium (31±3 meq/100g) and sodium (27±1 meq/100g). The predominant soluble ions are chloride, sulphate, bicarbonate and sodium.

The liquid limit of the bentonite is 102±4 %, the plastic limit 53±3 %, the density of the solid particles 2.70±0.04 g/cm^3 and 67±3 % of particles are smaller than 2 µm. The hygroscopic water content in equilibrium with the laboratory atmosphere (relative humidity 50±10%, temperature 21±3°C) is 13.7±1.3%.

The saturated hydraulic conductivity of compacted samples of the FEBEX reference bentonite is exponentially related to their dry density. Two empirical relationships relating hydraulic conductivity

(k_w, m/s) to dry density (ρ_d, g/cm^3) were obtained for samples permeated with deionised water at room temperature, valid each for a different dry density range (Villar 2002):

For $\rho_d > 1.47$ g/cm^3: $\log k_w = -2.96\ \rho_d - 8.58$ [1]

For $\rho_d < 1.47$ g/cm^3: $\log k_w = -6.00\ \rho_d - 4.09$ [2]

The swelling pressure (P_s, MPa) of compacted samples is also exponentially related to the bentonite dry density, according to the empirical expression in Eq. 3 (Villar 2002):

$\ln P_s = 6.77\ \rho_d - 9.07$ [3]

Relationships between suction and water content obtained for different bentonite dry densities under isochoric conditions can be found in e.g. Villar et al. (2019). For a sample compacted at dry density 1.6 g/cm^3 with hygroscopic water content the initial suction value would be ~120 MPa.

The pellets were prepared for the EB project (ENRESA 2005) using a 100-t batch of bentonite extracted in 2001 also from the Cortijo de Archidona deposit. To manufacture the pellets the bentonite was dried and milled in a multi-step process to produce a fine grade powder with a water content of between 3.0 and 4.5%. Later, a commercial plant with an in-line highly automated briquetting process produced coarse (7-15 mm) and fine (0.05-2 mm) grained materials with dry densities of 2.11 and 2.13 g/cm^3, respectively (Kennedy et al. 2004). Preliminary mineralogical analyses suggest that the content of smectite of this batch could be lower than in the FEBEX batch, whereas the quartz, calcite and dolomite contents would be higher. The cationic exchange capacity was also checked to be lower (Villar and Gómez-Espina 2012). A detailed hydro-mechanical characterisation of this mixture was performed by Hoffmann (2005).

The different grain sizes were kept separated in the laboratory and mixed in the right proportion just before every test, trying to keep a Fuller's curve similar to that used for the EB project, with a maximum diameter of 12.7 mm and a minimum diameter of 0.425 mm, in order to reduce

segregation. The precise granulometric distribution used in the laboratory tests is shown in Tab. 1. Except for the two first tests performed (MGR21 and MGR22) no pellets larger than 9.5 mm were used (the laboratory run out of them). In tests MGR23 to MGR27 the pellets were softly dried to a water content closer to the fabrication one (3.5%), because the water content of the pellets had increased during storage to a value of ~10%. This resulted in a significant different initial suction between the pellets that were dried and those that were not, 380 *vs*. 114 MPa (measured with a capacitive sensor).

Tab. 1. Granulometric curve of the bentonite pellets used in the tests (MGR and CW)

Sieve sizes (mm)	**Percentage retained (%)**	
Test	MGR21, MGR22	Rest of tests
9.5	17	0
4.75	31	37
2.0	26	31
1.18	11	13
0.59	10	12
0.425	5	6

2.2 Tests in large-scale oedometer

The large-scale oedometer consists of a cylindrical body with base and an upper piston that may move along the cylinder (Fig. 1). The body has an inner diameter of 10.0 cm and the length of the sample inside was 10.0 cm. The top and bottom of the sample were in contact with filter papers and ceramic porous discs connected to outlets. The cell was placed in a rigid frame that guaranteed the constant volume of the sample by hindering the displacement of the piston. An external LVDT measured the potential axial displacements, whereas a 10-t load cell in the upper part of the frame

measured the force developed by the specimen with a precision of 0.2% (equivalent to ±1 kPa for an axial pressure of 0.5 MPa). This cell was used in previous investigations using pellets or compacted powder separately (Imbert and Villar 2006, Villar 2012).

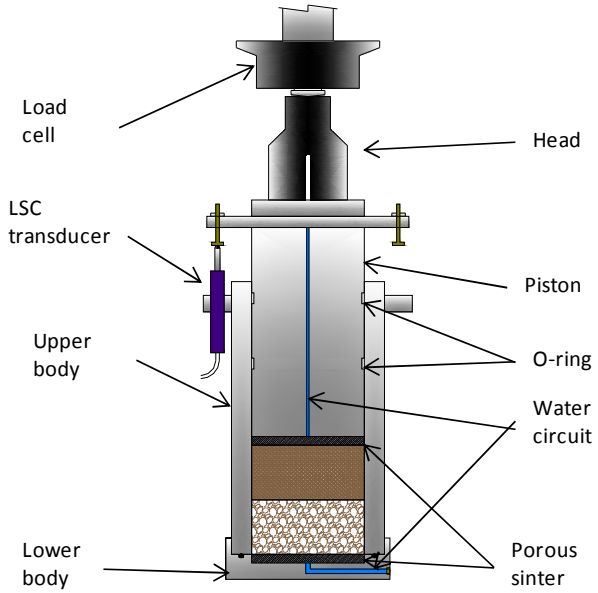

Fig. 1. Schematic representation of the oedometer cell

The lower half of the cell was filled with bentonite pellets with an average dry density close to 1.30 g/cm^3 and the upper part by a bentonite block of nominal dry density 1.60 g/cm^3, except in test MGR27, in which the position of block and pellets was inverted. The bentonite was directly compacted inside the cell with its hygroscopic water content. The pellets were poured on this block and carefully shaken as necessary to get the target density (Fig. SM1 in Supplementary Material, available online). Then the cell was overturned and mounted in the oedometric frame. The water intake took place thorough the bottom surface, either under a low injection pressure (a 1.5-m water column, 15 kPa) or under a constant low flow (0.05 cm^3/h). In the first case the water intake was measured with an automatic volume change apparatus and in the second case with a pressure/volume controller. During hydration the top outlet remained open to atmosphere and the pressure exerted by the material, the sample deformation and the water intake were measured and

automatically recorded. A summary of the tests performed and of their characteristics is given in Tab. 2 and Tab. 3.

Tab. 2. Characteristics of the MGR tests

Test	Hydration	Duration (days)	Observations	*T* (°C)
MGR21	Constant pressure: 15 kPa	34	Including pellets >9.5 mm	23.1±0.6
MGR22	Constant flow: 0.05 cm^3/h	266	Including pellets >9.5 mm	22.5±1.3
MGR23	Constant pressure: 15 kPa	210	Pellets dried	22.6±1.5
MGR24	Constant pressure: 15 kPa	14	Pellets dried	22.5±0.6
MGR25	Constant pressure: 15 kPa	76	Pellets dried	22.7±1.1
MGR26	Constant flow: 0.05 cm^3/h	132	Pellets dried	23.6±1.2
MGR27	Constant pressure: 15 kPa	278	Pellets dried	23.0±1.2

2.3 Tests in transparent cell

The transparent cell or window cell (CW) is a custom-built square cell consisting of two transparent methacrylate faces screwed to a steel frame (Fig. 2). The inner dimensions of the steel frame are 121x118x20 mm. A square block of the same dimensions was compacted in a bespoke mould and half sectioned. One of the halves was placed in the cell and the rest of the cell was homogeneously filled with the pellets while the cell was horizontally laid. Photographs of the mounting process are shown in Fig. SM2. During assembly the fine fractions moved towards the bottom. The side of the cell which was at the bottom during assembly was called B-face. Hence, the two faces of the cells, A and B, presented different appearance (Fig. SM3).

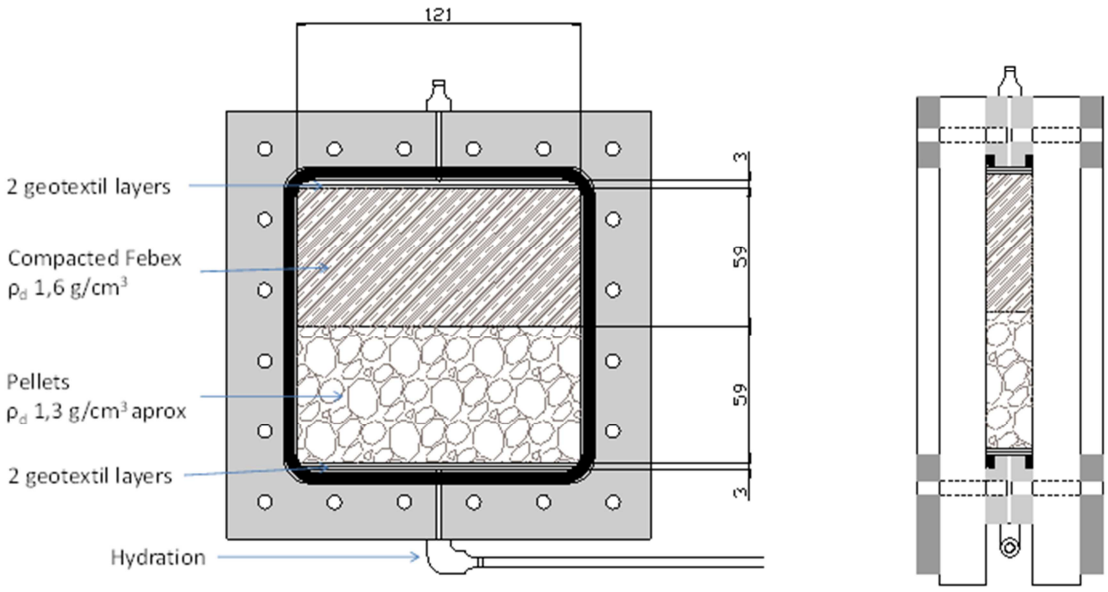

Fig. 2. Schematic front and lateral views of the transparent cell (CW1 with pellets at the bottom, as shown in the Figure, and CW2 with pellets on top)

Two geotextile layers were placed at the upper and bottom sides of the cell. Hydration took place through the bottom with a 30-cm (3 kPa) water column. In test CW1 the pellets were placed at the bottom, and inversely, in test CW2 the block was at the bottom and consequently was the first part to be hydrated. Photographs of both sides were periodically taken.

The tests were performed at room temperature (23±1°C). Test CW1 lasted 379 days and test CW2 lasted 420 days.

2.4 Postmortem analyses

At the end of the tests the samples were extracted from the cell (by pushing with a piston in the case of cell MGR), measured, weighed, and cut in regular horizontal sections. Each section was subsampled to determine water content, dry density and the pore size distribution. The cylindrical blocks from MGR tests were sliced in 6 horizontal levels (3 for pellets and 3 for block). The CW

samples were cut into 15 parts (5 rows and 3 columns). The subsamples were numbered from top to bottom, i.e. sample #1 was the one farther away from the hydration surface.

The gravimetric water content (*w*) is defined as the ratio between the mass of water and the mass of dry solid expressed as a percentage. The mass of water was determined as the difference between the mass of the sample and its mass after oven drying at 110°C for 48 hours. Dry density (ρ_d) is defined as the ratio between the mass of the dry sample and the volume occupied by it prior to drying. The volume of the specimens was determined by immersing them in a recipient containing mercury and by weighing the mercury displaced, considering a density of mercury of 13.6 g/cm^3.

The pore size distribution of subsamples was determined by mercury intrusion porosimetry (MIP). The samples were put in the ice condenser of a Telstar LioQuest equipment at -30°C for 3 hours. Subsequently, they were lyophilised for 22 hours at a temperature of -50°C under a vacuum of 0.2 mbar, so that to sublimate the water in the pores. Thereafter, they were heated at 25-30°C for 3 hours. These samples were kept in a desiccator until the MIP analysis. The porosimeter used was a Micromeritics AutoPore Series IV 9500, which allowed the exploration of pore diameters between 0.007 and 600 µm. Prior to mercury injection the sample was outgassed by applying a vacuum of 50 µm-Hg. Afterwards the mercury injection pressure was increased from 2.7 kPa to 220 MPa in 109 steps. To determine the extrusion branch of the curve, the pressure was released in 56 steps down to a pressure of 68.6 kPa. A contact angle of mercury of 139° both on advancing and of receding on the clay surface was considered.

The (001) reflection or basal reflection gives the distance along the crystallographic *c*-axis between clay lamellae and for a given clay mineral depends on the exchangeable cations present in the interlayer and their degree of hydration. To determine it, subsamples were preserved in paraffined foil after dismantling of the cells and the X-ray diffraction profile of a plane surface of them was registered at laboratory temperature after removing the foil and without any further treatment. An

anode of Cu (CuKα) radiation was used with a Philips model X'Pert-MPD diffractometer at 40 mA, 45 kV operating condition. The profiles were obtained with a 0.1-mm entrance slit and a scanning rate of 0.025°2θ/s. Data were collected between 2 and 10°2θ. The goniometer settings were: automatic divergence slit and diffracted beam slit 2 mm. In other samples, an anode of Cu (CuKα) radiation was used with a Bruker D8 Advance diffractometer at 40 mA and 40 kV operating conditions. XRD experimental profiles were obtained with a 1-mm entrance slit, 0.05°2θ step size and a counting time of 3 s per step. Data were collected between 2 and 30°2θ. The divergence slit and diffracted beam slit of the goniometer were fixed at 1 mm. In both cases the position of the diffraction peaks was adjusted by using the quartz in the samples as an internal standard. The complete mathematical description of the scan pattern was obtained by combination of a polynomial function that describes the background and a profile function that fits the experimental reflections. The pseudo-Voigt profile function was used to fit the diffraction peaks as well as to deconvolute overlapped reflections.

Additionally, in each CW test a cylindrical subsample was obtained by drilling across the block/pellet interface to measure the gas breakthrough pressure as an indicator of the sealing quality of the interface. This subsample was vertically crossed by the interface. The core diameter was fit to 3.8 cm by using a cutting ring and knife. Filter paper and porous stones were placed on top and bottom of the sample and it was laterally wrapped in double latex membranes. Vacuum grease was applied between membranes in order to prevent the loss of gas. The wrapped sample was placed in a triaxial cell which was filled with de-aired water and pressurized to ensure perfect adherence of the membranes to the surface of the sample and avoid gas transport along it. The cell inlet at the upper part of the sample was connected to a nitrogen gas cylinder applying the gas injection. The outlet of the cell connected to the bottom of the sample was open to atmosphere, with a series of different range gas mass flowmeters measuring the gas outflow. More experimental details about the equipment and the equations used to compute permeability are given in Villar et al. (2018, 2021). Gas was applied through face A (that of coarser granulometry, Fig. SM3). The particular test

procedure was adapted to the characteristics of the samples. In test CW1 the injection pressure was increased until outflow occurred and in test CW2 the confining pressure was increased until flow stopped.

3 Results

3.1 Hydration process

3.1.1 Large-scale oedometer: online measurements

Water intake, axial pressure and vertical deformation were continuously measured during hydration. Vertical deformation was minimal, since the movement of the piston was blocked by the oedometer framework. In fact the changes in overall dry density occurred as a result of the small vertical deformation allowed were in all cases below 0.005 g/cm^3. Fig. 3 and Fig. 4 show the evolution of water intake and axial pressure for the seven tests. The tests were stopped and dismantled after different periods of time to get the temporal evolution of the postmortem information detailed in sections 3.2.1, 3.3.1 and 3.4. Tests MGR22 and MGR23 continued until a pressure plateau was reached.

Fig. 3 also shows the water intake necessary to reach full saturation (250±12 g), which was not the same for all the tests because of the slight differences among them in initial dry density and water content (Tab. 3). Some of the tests reached full saturation. There was a significantly different behaviour between the tests performed under constant injection pressure (MGR21, MGR23, MGR24 and MGR25) and the tests performed under constant water inflow rate (MGR22 and MGR26). In the constant-pressure tests the water intake was very quick and more than half of the water volume necessary for full saturation was taken in about 20 days, which was probably caused by the high permeability of the pellets part. In contrast, the water intake was much slower in the two tests in

which constant flow was prescribed, and it took more than 100 days to reach overall degrees of saturation close to 50%. The water intake rate in test MGR27, in which hydration took place through the block part of the column (which was placed at the bottom), was initially intermediate between that of tests performed under constant pressure and those performed under constant inflow. However, it showed the slowest water intake rate in the long run, attesting the lower permeability of the higher density block. Some of the differences among the tests, particular concerning the initial water intake, were likely caused by experimental artefacts. In test MGR23 there was a short period (~14 days) during which no water was supplied to the cell because air entered the hydration line. As shown in Fig. 4, this did not affect the swelling pressure evolution.

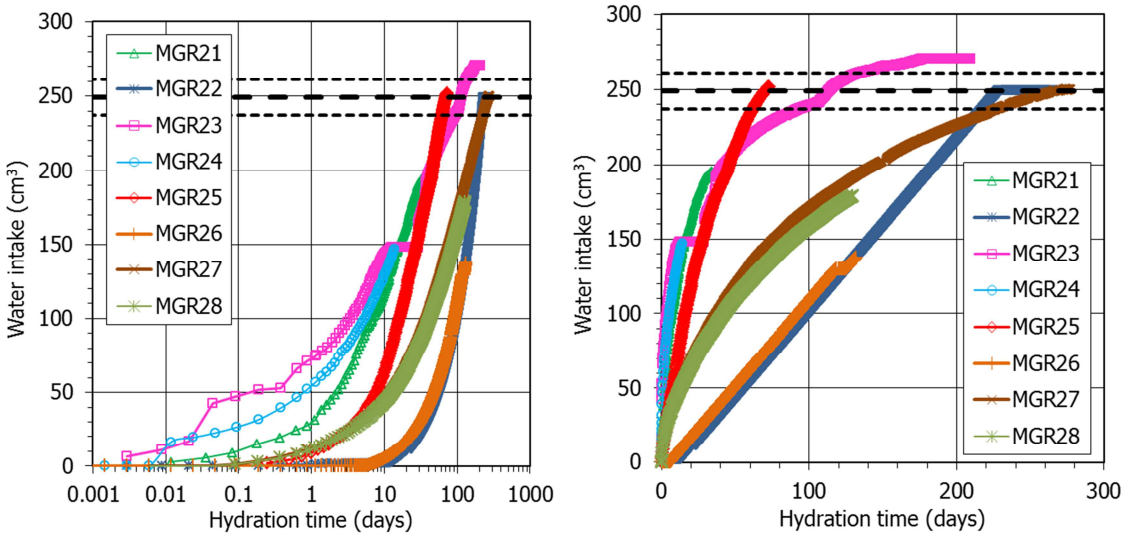

Fig. 3. Water intake evolution in the large-scale oedometer tests in log and linear temporal scales (constant flow was prescribed in tests MGR22 and MGR26). The thick horizontal lines indicate the water intake necessary to reach full saturation (average and standard deviation). In tests MGR22 and MGR26 the water intake includes partly the intake of the bottom porous stone (6-14 cm^3)

Fig. 4 shows the axial pressure development over time and as a function of the overall degree of saturation (Fig. SM4 shows the evolution of axial pressure over time in a linear temporal scale). The degree of saturation shown in Fig. 4 is an overall value for the two-component samples but, at any

given time, the actual degrees of saturation at different points along the sample height were very different, as the postmortem determinations presented in section 3.2.1 showed.

In terms of temporal evolution, the axial pressure build up was generally steep at the beginning. In the longer tests, after the initial peak there was a smooth decrease in axial pressure that eventually recovered and continued increasing after final stabilisation. The initial pressure peak occurred for overall degrees of saturation close to 80% in tests MGR23 and MGR25. In test MGR23 the period of time during which the axial pressure significantly increased with no change in the overall degree of saturation corresponds to the ~14 days period during which inadvertently no water was supplied to the cell. The fact that pressure continued to build up would indicate that water redistribution inside the bentonite can cause pressure increase. In contrast, in test MGR22, performed under controlled flow conditions, axial pressure peaked for an overall degree of saturation of only ~60%. This would mean that slow saturation was more efficient, in the sense that it allowed a better water redistribution inside the microstructure.

In the long test MGR23, after the sharp initial increase (the peak was reached at 30-40 days), there was an intermediate stage of slight pressure decrease, and when the average degree of saturation was ~90% the axial pressure steadily increased again until full saturation was reached, with a stable pressure value of 3 MPa. Test MGR22 also went on until full saturation was reached. Since in this test the inflow was very low and controlled, the pressure development kinetics was very different to the other tests. Axial pressure started to develop slightly later than in the other tests (after 10 days), and when the overall degree of saturation was much lower than in the other tests (37%). The first peak was reached after 80 days and the intermediate stage lasted until 200 days had elapsed. During this time the overall degree of saturation increased from 58 to 96%. In the final stage, the water injection pressure started to increase because the P/V controller was not able to keep a constant low injection flow into a quasi-saturated sample without increasing the injection pressure. As a result, there was a

new steep increase in axial pressure until the final value of 3 MPa. When the water injection pressure had increased to 1.5 MPa, water injection was stopped and the pressure was allowed to dissipate for 38 days. This explains the odd final shape of the curves for test MGR22. During this period of water injection pressure decline, the axial pressure did not change (Fig. 5).

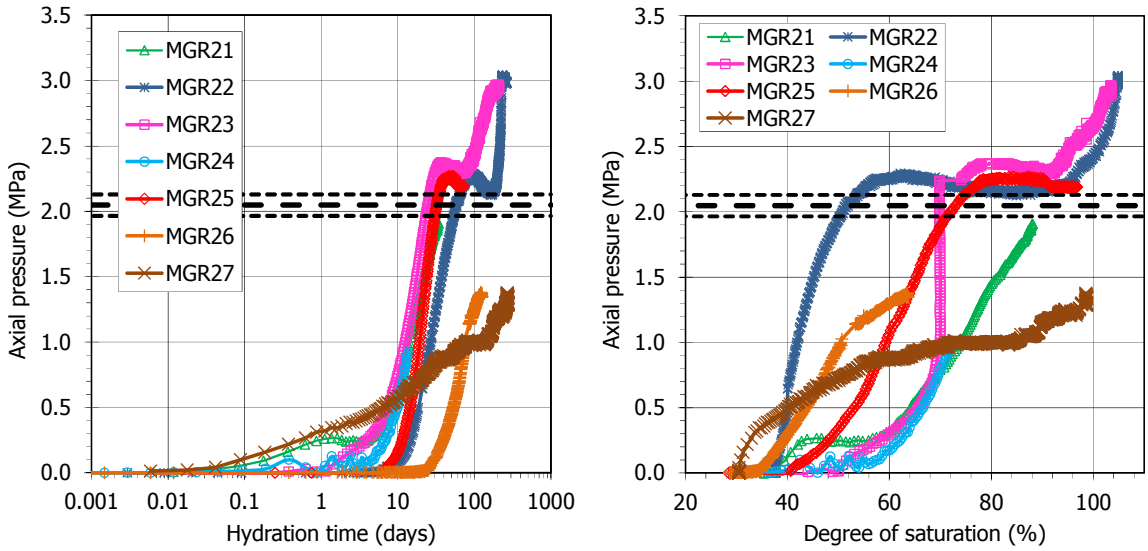

Fig. 4. Axial pressure evolution over time (left) and as a function of the overall degree of saturation (right) in the large-scale oedometer tests (constant flow was prescribed in tests MGR22 and MGR26). The thick horizontal lines indicate the expected swelling pressure according to Eq. 3 (average and standard deviation)

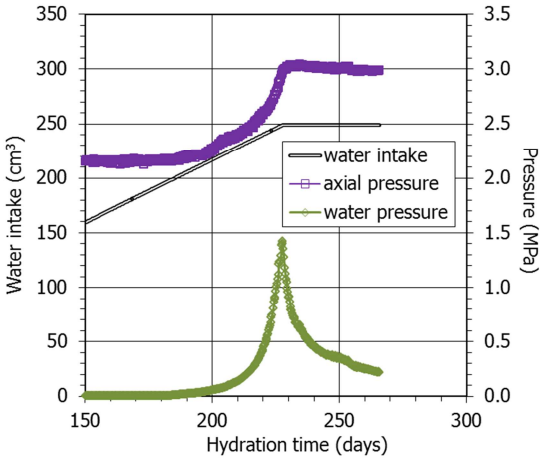

Fig. 5. Final stage of test MGR22

3.1.2 Transparent cell: visual observations

Cells CW1 and CW2 were photographed on both sides (A and B faces) periodically during hydration. Fig. 6 shows a comparison of the appearance of face A of the two tests at the same testing times (and Fig. SM5 for face B). Variations in the coloration of the grains, changes in texture and shape, and displacement of the block-pellets interface were observed. As the pellets were hydrated, the grains increased in size, without displacement, and the whole of them lose sharpness. The appearance of the saturated pellets was gel-like. The evolution of hydration was slower in face B, where fine particles predominated. The reason could be the absence of large voids where water could quickly and easily penetrate. A downwards movement of the pellets/block interface in cell CW1 was observed, whereas this interface moved upwards in cell CW2.

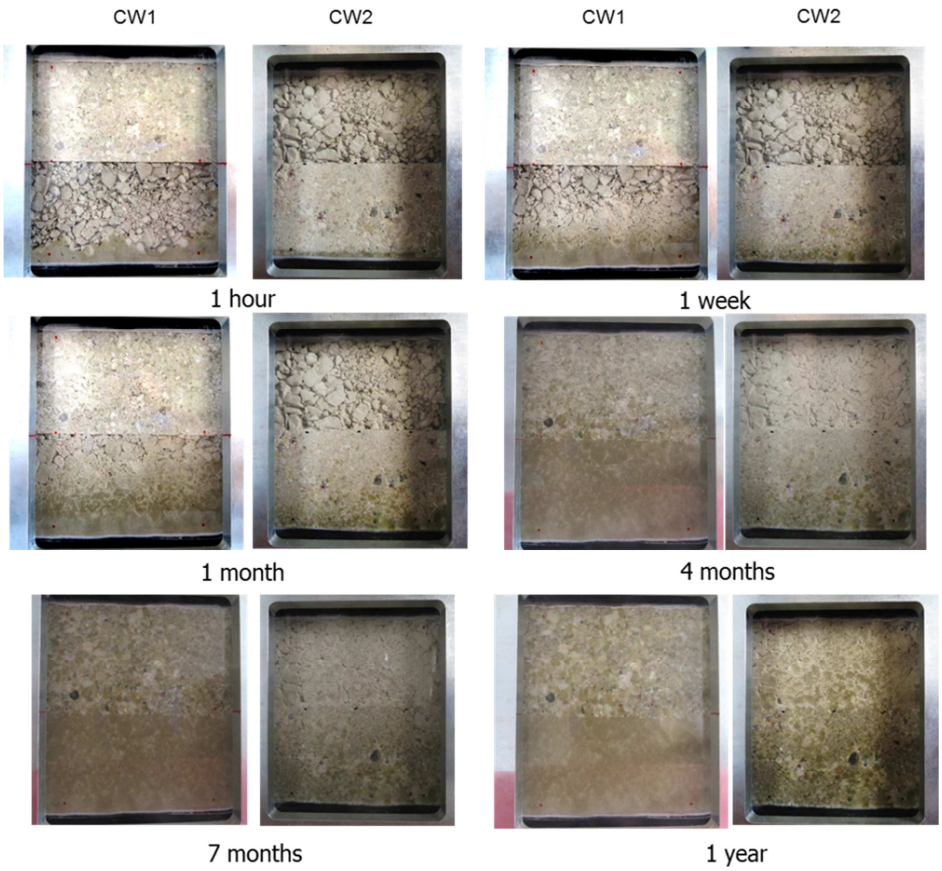

Fig. 6. Comparison, in face A, of the evolution of the hydration fronts in both cells (CW1: first and third column, and CW2: second and fourth column) for six different moments

3.2 Final physical state

3.2.1 Large-scale oedometer

The tests were dismantled after different running times. The final appearance of the samples once extracted from the cell is shown in Fig. 7 for the tests performed hydrating from the pellets half under constant injection pressure and in Fig. 8 for the rest of tests. The sample from the shorter test (MGR24) showed a quite saturated bottom in which the pellets could not be told apart, but the upper part of the pellets half still showed open voids. The two halves of this sample (pellets and block) could easily be detached. In the other cases the two halves were sealed and had to be separated with a knife. Already after 76 days the pellets half looked homogeneous. In contrast, in the tests performed under constant inflow rate, after 132 days (test MGR26) some pellets could still be told apart. In test MGR27 (saturated through the block), although the block looked saturated, the pellets upper part still presented voids from the initial fabric.

Fig. 7. Appearance of the MGR samples at the end of the tests performed under constant water injection pressure

Fig. 8. Appearance of the MGR samples at the end of the tests performed under constant water inflow rate (MGR22, MGR26) and with saturation through the block (MGR27)

Once extracted the blocks were weighed, measured and horizontally sectioned to determine the longitudinal changes in water content, dry density and pore size distribution. Tab. 3 shows a summary of the final characteristics of the samples, along with the initial values. The original height of the halves changed during the tests: the height of the bottom, pellets half decreased whereas the height of the upper, block half increased, indicating the increase in the overall dry density of the pellets and decrease in the dry density of the block. These changes are illustrated in Fig. 9 and were confirmed by the postmortem determination of dry density in the six horizontal sections. The water content of the bottom part (pellets) increased very quickly, but over time tended to decrease. In contrast, the dry density of the pellets half increased in a more continuous way. The behaviour of test MGR26 performed under constant flow (lasting 132 days) did not follow the overall trend, since the increase in water content was moderate and similar for both halves, attesting the more homogeneous water redistribution allowed by slow hydration. The two longest tests, which were performed under constant water inflow (MGR22) or with the block at the bottom (MGR27) should be separately considered. When hydration took place through the block, the final water content and dry density of both halves were more homogeneous.

Tab. 3. Initial and final characteristics of MGR tests

	Initial				Final			
	w **(%)**	***h*** **(cm)**	ρ_d **(g/cm^3)**	S_r **(%)**	***w*** **(%)**	ρ_d **(g/cm^3)**	***h*** **(cm)**	S_r **(%)**
Test	MGR21, 34 days							
Pellets	9.5	4.97	1.26	23	35.9	1.31	4.80	91
Block	13.3	5.01	1.60	52	22.9	1.50	5.33	78
Total[a]	11.6	9.98	1.43	35	29.0	1.43	10.00	88
Test	MGR22, 266 days							
Pellets	9.9	5.04	1.28	24	35.3	1.35	4.79	95
Block	13.6	4.94	1.61	55	30.7	1.51	5.27	106
Total[a]	11.9	9.98	1.45	37	32.7	1.44	10.01	101
Test	MGR23, 210 days							
Pellets	3.5	5.00	1.30	9	35.7	1.34	4.84	95
Block	14.2	4.98	1.60	56	31.1	1.51	5.29	107
Total[a]	9.4	9.98	1.45	29	33.2	1.45	10.01	103
Test	MGR24, 14 days							
Pellets	5.7	5.02	1.28	14	31.0	1.30	4.93	78
Block	13.7	4.97	1.62	55	16.2	1.57	5.13	61
Total[a]	10.1	9.99	1.45	32	23.0	1.45	10.00	72
Test	MGR25, 76 days							
Pellets	3.2	4.99	1.30	8	37.0	1.33	4.88	97
Block	14.1	5.00	1.59	54	26.7	1.51	5.24	92
Total[a]	9.2	9.99	1.44	29	31.4	1.44	10.02	97
Test	MGR26, 132 days							
Pellets	3.5	5.01	1.30	9	21.0	1.32	4.92	54
Block	13.9	4.99	1.60	55	20.6	1.49	5.35	69

	Initial				Final			
	w (%)	h (cm)	ρ_d (g/cm^3)	S_r (%)	w (%)	ρ_d (g/cm^3)	h (cm)	S_r (%)
Total[a]	9.2	10.00	1.45	29	20.8	1.44	10.07	64
Test	MGR27, 278 days							
Pellets	3.0	5.00	1.31	8	32.3	1.43	4.55	99
Block	15.3	5.00	1.59	59	30.0	1.45	5.47	94
Total[a]	9.8	10.00	1.45	30	31.7	1.45	10.02	99

[a] the initial values are the averages of block and pellets, the final values correspond to online measurements (except in test MGR22)

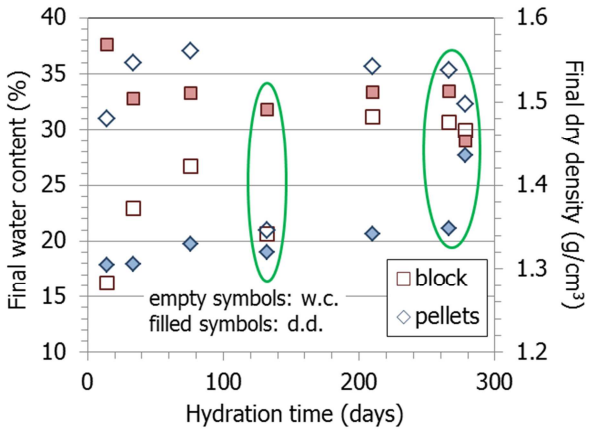

Fig. 9: Final average water content and dry density of the block and pellet halves of the samples (the values circled correspond to tests performed under constant inflow rate (MGR22, MGR26) or with the block at the bottom (MGR27)

The water content and dry density values measured in subsamples are plotted in Fig. 10 as a function of the distance to the hydration surface. The initial values are indicated with thick horizontal lines. The differences in the initial water content of the pellets were caused because in tests MGR23 to MGR27, prior to mounting, the pellets were dried to the values they had after they were manufactured (Tab. 2). During the tests the water content and degree of saturation decreased from the hydration surface (sample bottom) upwards whereas the dry density increased. These gradients

attenuated over time, hence they were smoother as the test duration was longer. The pellets/block interface did not seem to have any effect on the continuous gradients. The final dry density and water content values were similar in tests MGR22 and MGR23, despite the different hydration conditions (constant flow or pressure). Although the bentonite was finally fully saturated, the dry density and water content along the samples did not completely equalise. In contrast, test MGR26, which was far from full saturation, showed a quite homogeneous water content distribution, whereas the difference between the dry density of pellets and block was still significant.

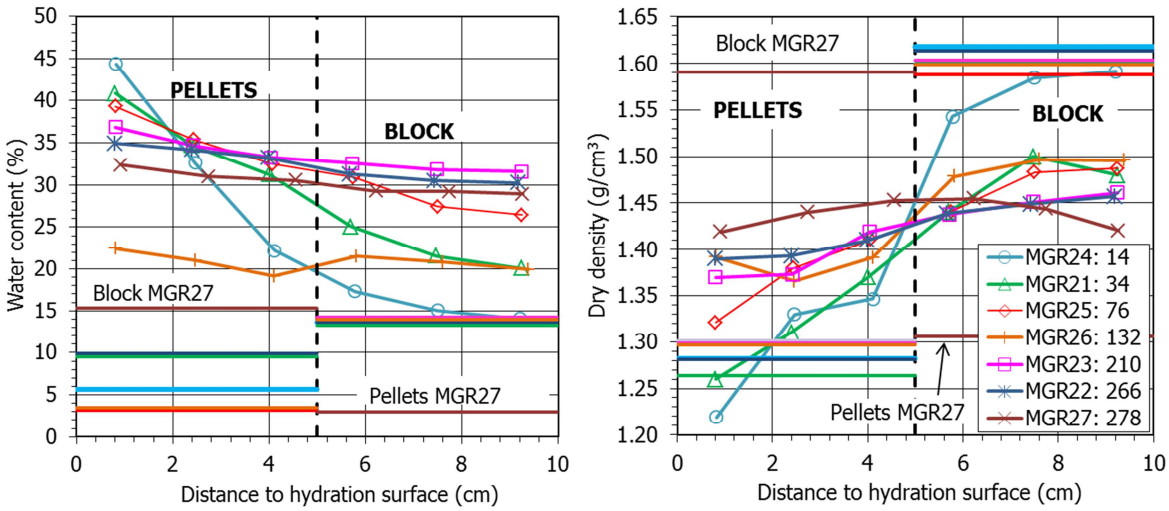

Fig. 10. Final water content and dry density along the samples of MGR tests. The duration of the tests is given in days in the legend. The thick horizontal lines mark the initial values

3.2.2 Transparent cell

Cell CW1, saturated through the pellets, was dismantled after 379 days and cell CW2, saturated through the block, after 420 days of hydration. A detailed characterisation of the final state of the bentonite was carried out in subsamples taken according to the schema shown in Fig. 11. It was not possible to distinctly separate the block and pellet parts. Tab. 4 summarises the initial and final characteristics of the tests. For the global values, the initial and final dimensions and weight of the pellets/block assemblage were considered. Because bentonite swelling caused the compression of

the geotextiles placed on top and bottom of the cell (Fig. 2), the total height of the sample increased and hence there was an overall decrease in dry density. Cell CW1 had reached full saturation, but not cell CW2, despite its longer duration. The values shown in the Table for the block and pellets parts are the average of the determinations in subsamples. These may be affected by trimming and slight drying during manipulation.

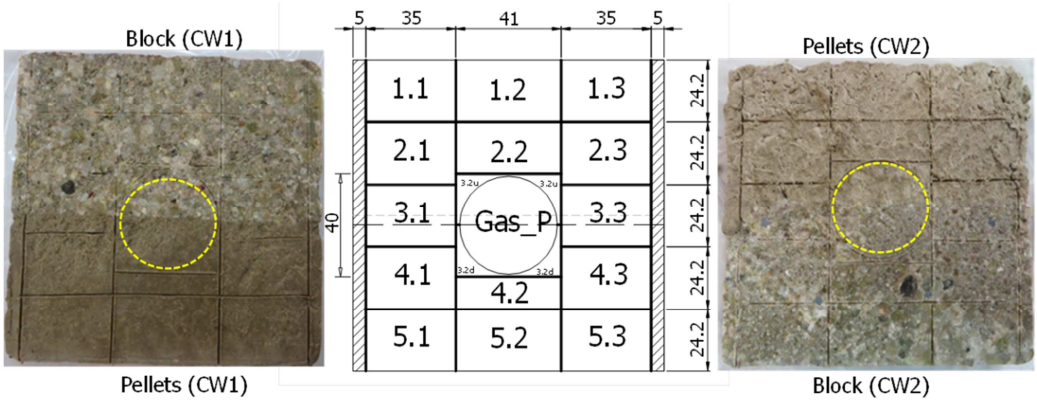

Fig. 11. Final subsampling of tests CW and location of samples for gas permeability (circle)

Tab. 4. Initial and final characteristics of tests CW1 and CW2

Test		Initial				Final			
		h (cm)	*w* (%)	ρ_d (g/cm^3)	S_r (%)	h (cm)	*w* (%)	ρ_d (g/cm^3)	S_r (%)
	Pellets[a]	5.75	10.1	1.30	25	5.69	40.5	1.28	99
CW1	Block[a]	6.03	14.0	1.59	54	6.37	32.8	1.47	105
	Total[b]	11.79	11.9	1.45	37	12.06	35.9	1.38	102
	Pellets[a]	5.60	10.1	1.30	25	5.58	32.4	1.31	82
CW2	Block[a]	5.98	12.4	1.61	50	6.64	32.1	1.45	101
	Total[b]	11.58	11.2	1.46	36	12.22	32.1	1.39	92

[a] final dry density and degree of saturation affected by subsampling and trimming, [b] final values affected by compression of geotextile during test

Fig. 12 shows the final water content and dry density determined in the subsamples of the two tests, along with the initial values. Hydration resulted in an overall water content increase both in the pellets and the block parts, considerably higher for the pellets part of test CW1. As a result of the water content increase, the bentonite swelled and the dry density of the assemblage decreased because of the slight deformation allowed by the geotextile compression (the overall dry density of cell CW decreased from 1.45 to 1.38 g/cm^3 and that of cell CW2 from 1.46 to 1.39 g/cm^3). In both tests the swelling was higher in the block part, whose dry density significantly decreased. Despite the fact that the sample CW1 was fully saturated at the end of the test (Tab. 4), there were still clear water content and dry density gradients, with higher water contents and lower dry densities in the pellets part, which was earlier saturated. In contrast, cell CW2, which was not completely saturated, showed homogeneous water content but still considerably higher dry densities and degrees of saturation in the block part. In fact, the average degree of saturation of the pellets part was only of 82%. The interface between pellets and block did not seem to play any role in the general trend of these variables.

However, a small border effect was observed at the bottom of the cells: the water content of the subsamples close to the border (5.1 and 5.3 in Fig. 11) was higher than that of the middle subsample (5.2), whereas the dry density was lower, especially in cell CW1. The cell border effect persisted, although weakened, until the upper part (e.g. samples 1.1 and 1.3 had slightly higher water content and lower dry density than sample 1.2).

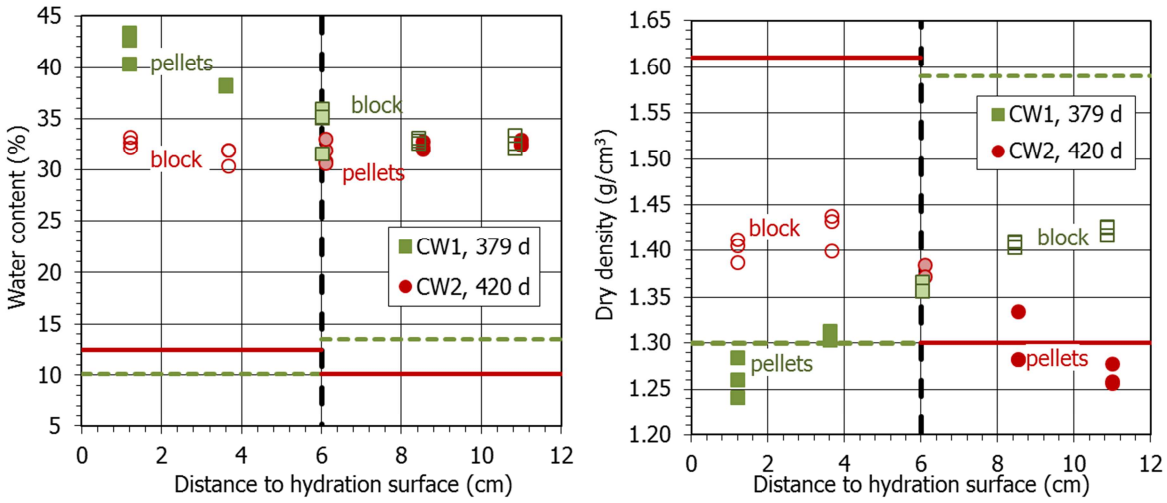

Fig. 12. Final water content and dry density along the samples of CW tests. The duration of the tests is given in days. The thick horizontal lines mark the initial values (discontinuous lines for CW1)

3.3 Pore size distribution

The pore size distribution of the samples was determined by mercury intrusion porosimetry (MIP). In some subsamples duplicates were tested. In the sections below, the intrusion curves obtained in some of the samples are shown. In all of them the usual two pore families of compacted FEBEX bentonite corresponding approximately to pores larger and smaller than 200 nm could be told apart. This limit is not the same as that between macropores and mesopores, which according to the classification of Sing et al. (1985) would be at 50 nm. There is also discussion on the criteria that can be followed to select this delimiting value (Yuan et al. 2020). The 'valley' criterion was chosen in this work, consisting of using the lowest point of the valley between the two peaks of a bimodal distribution. In several THM models, this pore size represents the limit separating inter-aggregate from intra-aggregate pores, the latter not affected by density changes (e.g. Lloret et al. 2003, Sánchez et al. 2005, Mašín 2013).

The mercury intrusion method allows access to be gained only to part of the macroporosity (pores of diameter smaller than ~550 µm) and to part of the mesopores (those of diameters larger than 7 nm),

since mercury does not intrude the microporosity (pores of a size of less than 2 nm, according to the same classification mentioned above). Actually, the percentage of pores intruded by mercury in the samples analysed in this work was between 30 and 76%. Considering that most of the non-intruded porosity corresponds to the pores of a size smaller than the limit of the apparatus (7 nm), an estimation of the percentage of pores actually intruded can be made by comparing the actual void ratio of the samples (*e*, computed from their dry density and density of solid particles) and the apparent void ratio calculated from mercury intrusion (*e**). There is uncertainty in this approach, since it is possible that pores larger than 7 nm were not intruded because of the bottleneck effect: the pores connected to the external surface by narrow openings will not be intruded until sufficient pressure is applied to intrude the entryways. All of the volume of such pores will be allocated to the threshold radius class of the most restricted part of the entryway, which will result in an overestimation of the smaller pore sizes volume. Likewise, although in compacted clay materials pores larger than those that can be quantified by MIP are not expected, pores of this size could be present in some of the driest pellets samples.

The intrusion curves of the subsamples are presented below along with the curves for FEBEX samples of the same characteristics as the initial conditions used in the cells. For the block part, the curve corresponding to a sample compacted at dry density 1.59 g/cm^3 with a water content of 14% was used as representative of the initial state. For the pellets, mixtures of pellets having approximately a Fuller's curve grain size distribution, with a resulting dry density of 1.29 g/cm^3 and water contents of 10 and 3% were used. The initial pellets curves showed a predominant pore size around 300 µm. Despite the low density of the pellets mixtures, the percentage of non-intruded porosity in them was very high (~70%). In this case not all the non-intruded porosity can be ascribed to pores smaller than 7 nm, because in the dry, low-density pellets mixture large pores are also to be expected. Hence, an estimation of the volume of pores larger than 550 µm has been made following this approach:

At the beginning of a MIP test the calibrated sample holder is filled with mercury under a low injection pressure. Considering the sample mass and the volumes of the sample holder and of mercury intruded, the dry density of the sample is computed by the equipment software. This initial mercury injection is considered by the equipment as the zero value for the rest of the MIP test, which actually starts when injection pressure is increased above this value. Thus, all the large porosity filled during this initial step is disregarded. The comparison between the dry density determined by the equipment at this step and the actual dry density of the sample allows computing the volume of pores larger than 550 µm: when the sample contains a significant volume of large pores, the dry density determined by the porosimeter is considerably higher than the actual dry density of the sample, whereas if there are not large pores the two values tend to be similar. Hence, in the dry pellets samples this difference was quite large, whereas in the saturated and high-density samples the differences found were not significant. This correction was done to the initial GBM and to those samples whose visual inspection clearly showed that contained large pores, namely samples MGR24-4, MGR24-5, MGR21-4 (Fig. 7) and all the pellets samples from tests MGR26 (Fig. 8) and CW2. The subsamples were numbered from top to bottom, i.e. sample #1 was the one farther away from the hydration surface.

Taking all the above into account, the void ratio corresponding to pores larger and smaller than 200 nm (e_M and e_m, macro and micro, respectively) was recalculated, assuming that the non-intruded porosity corresponded to pores smaller than the equipment injection capacity and, in some pellets samples, also to pores larger than 550 µm.

3.3.1 Large-scale oedometer test

As an example, Fig. 13 and Fig. 14 show the incremental curves of mercury intrusion for the subsamples of the tests lasting 14 (MGR24) and 210 days (MGR23). In the shorter test (Fig. 13) the pore size distribution of the subsamples taken from the block half was similar to that of the initial

block. Indeed, no relevant changes in the dry density and water content of the block samples took place during the oedometer test (only noticeable for the sample closest to the interface, 3b), because it was too short. This similarity proves the reliability of the technique. In contrast, the pore size distribution of the pellet half significantly changed. The size of pores larger than 200 nm and their volume decreased with respect to the initial pellets mixture. A similar pattern was found in test MGR21 (34 days). Overall, for the pellets subsamples of all the tests, the volume of pores larger than 200 nm significantly decreased, and the mean size of these macropores decreased from the initial ~300 μm to values mostly between 10 and 100 μm. This can also be observed in Fig. 14 for the subsamples from the pellets half of the longer test (MGR23). In contrast, the mean size of the pores smaller than 200 nm increased with respect to the original values for all the pellets subsamples, as well as for the block subsamples (Fig. 14 and Fig. SM6 for a summary of all the tests). Furthermore, in the block subsamples the volume and size of the macropores also increased, except in the shorter, less saturated tests. This overall increase in the pore volume of all the size ranges for the block subsamples is related to the decrease in the global dry density of the block parts during the tests (Fig. 9).

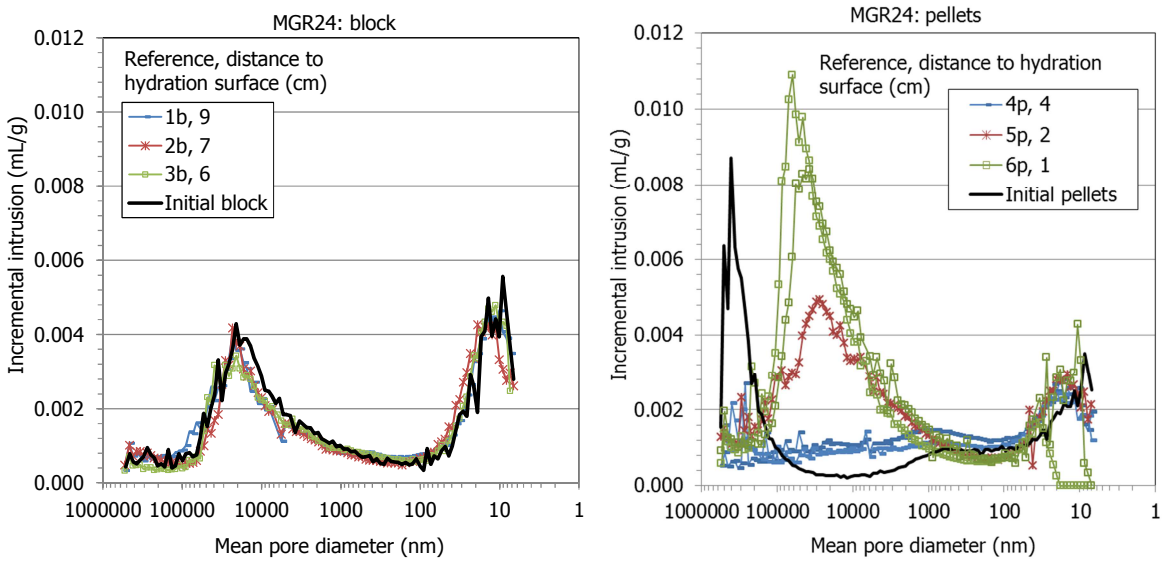

Fig. 13. Pore size distribution expressed as incremental mercury intrusion of samples from test MGR24 (lasting 14 days), corresponding to the block (left) and pellets (right) halves. The curves for the initial materials (blocks and pellets) are included

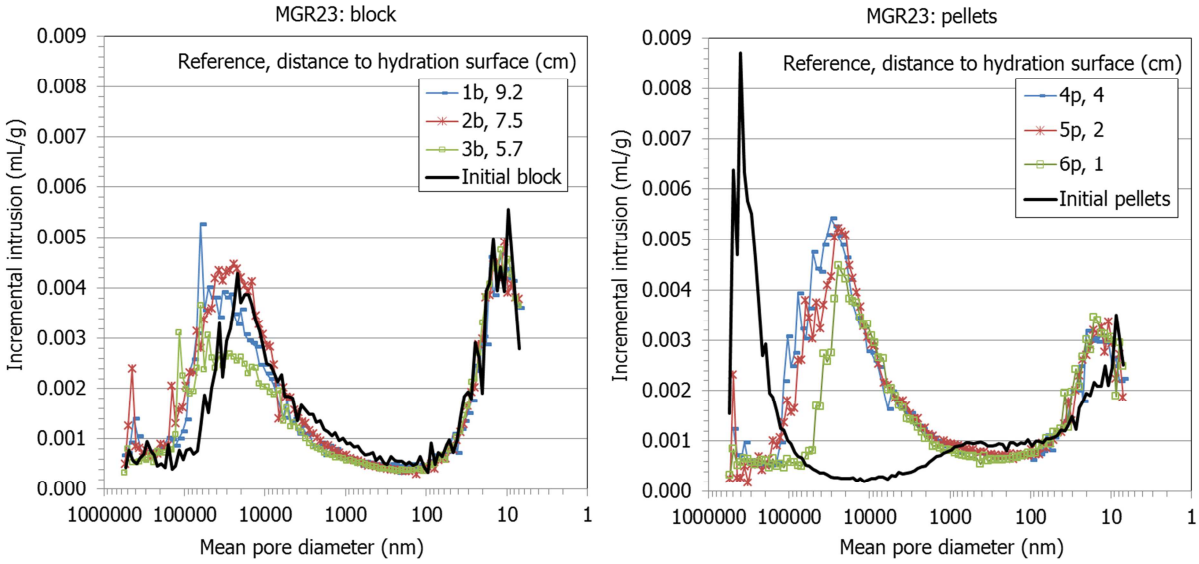

Fig. 14. Pore size distribution expressed as incremental mercury intrusion of samples from test MGR23 (lasting 210 days), corresponding to the block (left) and pellets (right) halves. The curves for the initial materials (blocks and pellets) are included

The void ratio corresponding to pores larger and smaller than 200 nm was recalculated as explained at the beginning of section 3.3. The ratio between the void ratio corresponding to pores smaller (e_m)

and larger (e_M) than 200 nm increased in all samples with respect to the reference values, which reflects the increase in the volume of micropores as a result of hydration (Fig. 15). This increase was much more significant for the pellets subsamples, except in the driest ones. In the block samples the largest proportion of void ratio corresponded to the pores of diameter smaller than 200 nm, and in fact for each test the largest e_m/e_M values tended to be in the block samples. The highest homogeneity in terms of e_m/e_M was reached in test MGR27, saturated through the block, which also had the most homogeneous dry density.

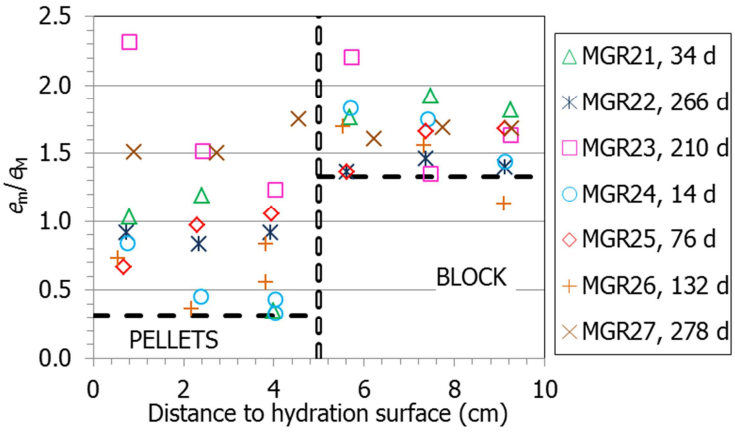

Fig. 15. Ratio between void ratio corresponding to pores smaller and larger than 200 nm (e_m and e_M) obtained by MIP in subsamples from the MGR tests (the thick horizontal lines indicate the initial conditions for all the tests except MGR27, in which the position of pellets and block was inverted)

3.3.2 Transparent cell

Fig. 16 shows the incremental curves of mercury intrusion as a function of the mean pore diameter of the diameter size intervals corresponding to each pressure increase step. In both tests the macroporosity of the pellets shifted to smaller pore sizes, more as the water content was higher. In particular, for the pellets part in test CW1 the mean size of the macropores considerably decreased, from ~300 µm to values between 6 and 40 µm. However, in some cases, pores larger than ~70 µm remained, particularly in CW2, where the pellets part was not completely saturated. The pore size

distribution of the block parts did not change much as a result of hydration, particularly in test CW1. In the block part of test CW2 the size and volume of the macropores increased. All the samples had mean pore diameters for the pores smaller than 200 nm in a narrow range between 6 and 26 nm, and in test CW1 tended to decrease away from the hydration surface. In general the mean size of this pore family was higher than that for the initial block.

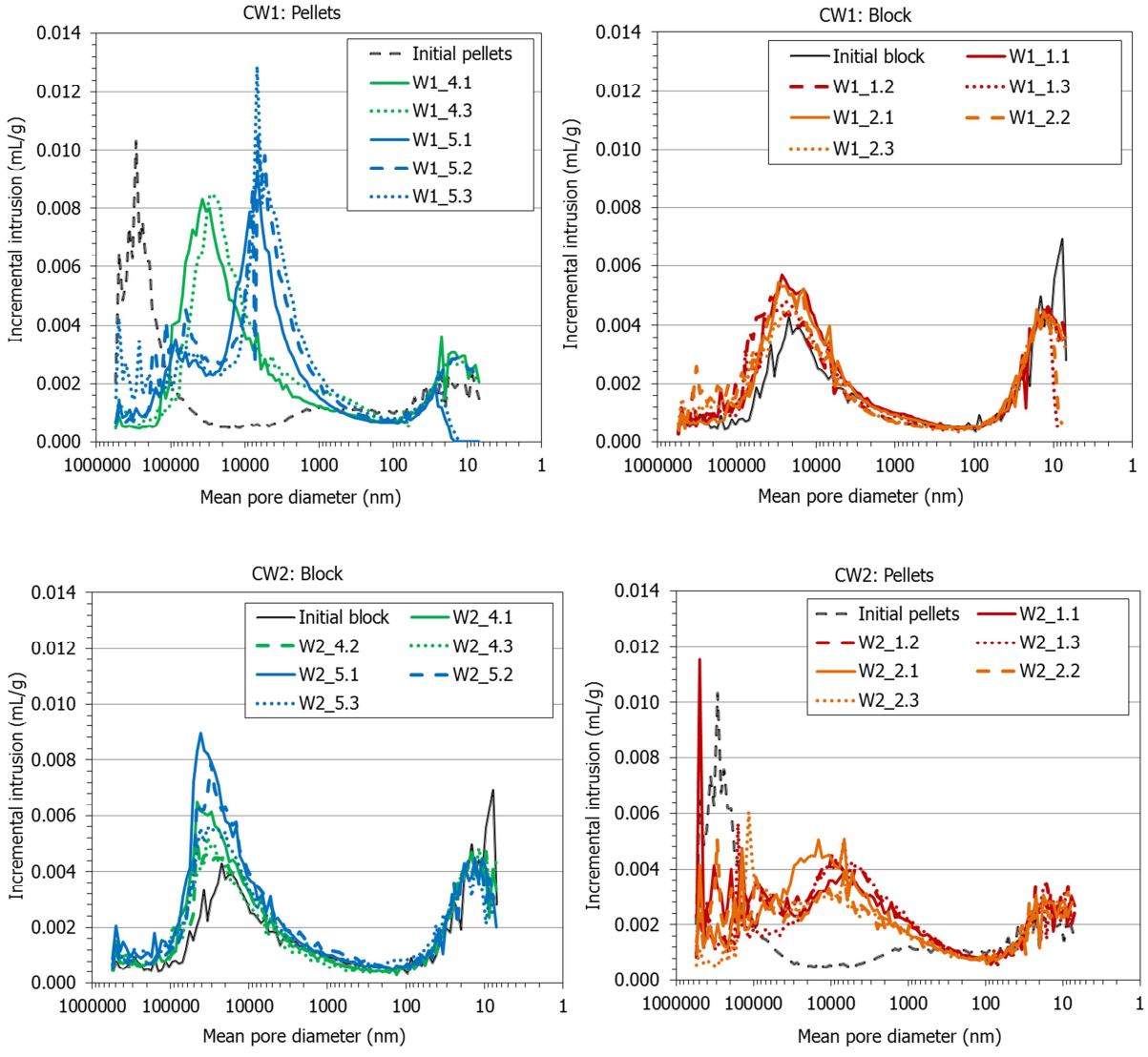

Fig. 16. Incremental mercury intrusion in tests CW1 and CW2 (the curves corresponding to the initial conditions are also included)

The ratio e_m/e_M obtained by MIP for the different subsamples is shown in Fig. 17 as a function of the distance to the hydration surface. For the pellets part in test CW1 the void ratio corresponding to pores larger than 200 nm considerably decreased, particularly away from the hydration surface. As a result, the e_m/e_M ratio increased in the same direction. In the pellets part of test CW2, the volume of large pores decreased only in some samples (except close to the pellets/block interface, where it significantly decreased), but the volume of pores smaller than 200 nm tended to increase, resulting in an increase of the e_m/e_M ratio in this area. In the block samples of both tests the largest proportion of void ratio corresponded to the pores of diameter smaller than 200 nm ($e_m/e_M>1$), but both e_m and e_M increased with respect to the initial values, reflecting the overall decrease in dry density allowed by the compression of the geotextiles as a result of bentonite swelling (Tab. 4). Hence the e_m/e_M ratio did not change much in the block parts of any of the tests, except for the samples closest to the hydration surface of test CW2, where it decreased.

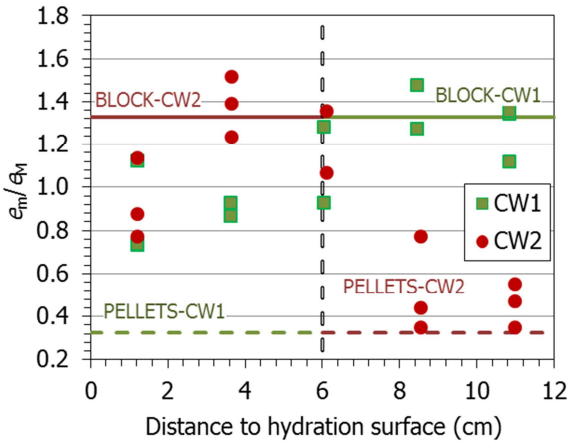

Fig. 17. Void ratio corresponding to different pore sizes obtained by MIP in samples from tests CW (the thick horizontal lines indicate the distribution for the reference block and pellets)

3.4 Interlayer space

The basal reflection of the subsamples after some MGR tests was determined by XRD. Fragments of the samples were X-rayed the same day in which the cells were dismantled, trying to keep the final

water content unchanged by avoiding any accidental drying. The results obtained showed that the (001)-reflection was a double one that could be decomposed into two diffraction peaks by profile fitting of the XRD patterns. In the case of the block samples the main diffraction peak corresponded to the full development of the 2-layer hydrate (~1.5-1.7 nm) and the secondary one to the 3-layer hydrate (~1.8-1.9 nm), whereas in the pellets samples the main diffraction peak corresponded to the full development of the 3-layer hydrate and the secondary peak was higher (2.0-2.1 nm). However, the samples from test MGR24, the shortest one, showed a single diffraction peak for the (001)-reflection at much lower values.

Fig. 18 shows the values corresponding to the main reflections. The initial basal reflection for the pellets samples would be ~1.3 nm, and for the compacted block ~1.5 nm. For a given test, no matter its duration, the final values were higher in the pellets part. For the pellets samples with water content higher than 30% the values were all above 1.8 nm, practically corresponding to the 3 water layer hydration state of the smectite. In contrast, block samples of similar water content had lower basal spacings.

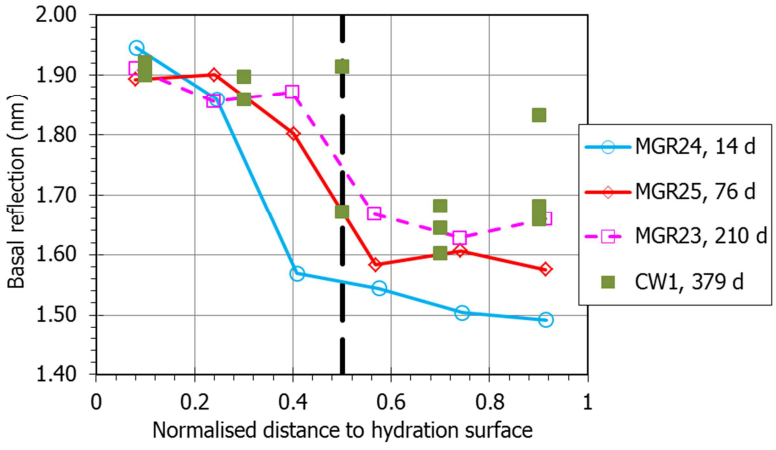

Fig. 18: Main diffraction peak of the basal reflection of subsamples of MGR and CW tests (total length of 10 cm in tests MGR and 12 cm in CW). Hydration took place through the pellets except in tests MGR27 and CW2. The duration of the tests is indicated in days

3.5 Healing of block/pellets interface: gas testing

At the end of the tests in transparent cell, a cylindrical subsample was obtained by drilling across the pellets/block interface to measure the gas breakthrough pressure as an indicator of the healing of the interface. These subsamples were vertically crossed by the interface (Fig. 11) and had a nominal diameter of 3.8 cm. The initial and final characteristics of the samples as well as those of the tests are shown in Tab. 5.

Tab. 5. Characteristics of the samples before and after gas testing and characteristics of the tests

Test	CW1-gas		CW2-gas	
	Initial	Final	Initial	Final
ρ_d (g/cm^3)	1.33	1.43	1.36	1.40
h (cm)	2.16	2.13	2.15	2.15
ϕ (cm)	3.78	3.68	3.79	3.73
w (%)	34.8	32.2	30.3	29.3
S_r (%)	92	99	83	85
Confining *P* (MPa)	3.0		1.1-2.3	
Injection *P* (MPa)	0.2-2.9		0.2-0.3	
Duration (days)	32		4	

In test CW1-gas a confining pressure of 3 MPa was applied, corresponding to the swelling pressure of the bentonite with a dry density of 1.45 g/cm^3 (the global value for test CW1) according to Equation 3. This value was selected to keep approximately the same stress state as the bentonite likely had at the end of the test, when almost full saturation was reached, and prevent the interface from mechanically splitting. The injection pressure was increased 0.1 MPa every two hours, from 0.2 to 2.95 MPa. There was no flow until the injection pressure reached 2.00 MPa. For injection pressures

from 2.00 to 2.24 MPa there were barely measurable flow pulses. There was again no flow until 2.85 MPa of injection pressure. For gas injection pressure of 2.90 MPa unsteady flow pulses close to the turndown value of the flowmeters were detected. At the end of the test the sample had consolidated as a result of the confining and gas pressure applied and its water content had slightly decreased, which would indicate that some water movement took place during the test.

It can be considered that the gas breakthrough pressure was ~2.2 MPa, although no steady, correctly measurable flow was measured at any moment. This breakthrough pressure would be in the order of the values expected for FEBEX samples compacted to dry densities between 1.35 and 1.45 g/cm^3, which would be between 1.5 and 3.5 MPa (Gutiérrez-Rodrigo 2018, Gutiérrez-Rodrigo et al. 2021).

Because the sample from test CW2 was not saturated, the confining pressure applied during gas testing was initially lower, 1.1 MPa. In this case the outflow was high from the first step of injection pressure (0.2 MPa), and the confining pressure had to be increased to reduce it. Outflow continued until the confining pressure was 2.3 MPa, for which pressure no flow occurred. Then the injection pressure was increased to 0.3 MPa, flow resumed and the test was dismantled. The permeability values obtained for each pressure step are shown in Fig. 19. They are expressed as $k_{rg}{\cdot}k_{ig}$, where k_{rg} is the relative gas permeability and k_{ig} is the intrinsic permeability measured with gas flow. The duration of the steps had some influence on the values obtained, because the sample consolidated as a result of the confining pressure application, which resulted in a decrease of gas permeability. This would explain the significantly lower value obtained in the last step, after the sample had been submitted to a confining pressure of 2.3 MPa for one day. Indeed the sample dry density increased during the test, even though the total duration of the test was of only 4 days. In particular, the permeability value obtained for a confining pressure of 0.1 MPa was $8{\cdot}10^{-17}$ m^2. These values are lower than those expected for the FEBEX bentonite compacted with similar accessible void ratio (i.e. void ratio accessible for gas flow, $e(1\text{-}S_r)$, in this sample 0.165). According to the correlation presented in Villar et al. (2013), for a sample of FEBEX bentonite compacted at the same accessible

void ratio, with no interface in it and tested under the same confining pressure, the intrinsic permeability should be ~$2 \cdot 10^{-15}$ m^2, i.e. considerably higher. This would indicate that the pellets/block interface was not a preferential gas pathway and flow took place through the bentonite whole porosity. Hence, the interface was perfectly healed and sealed, even though full saturation had not been reached in this area.

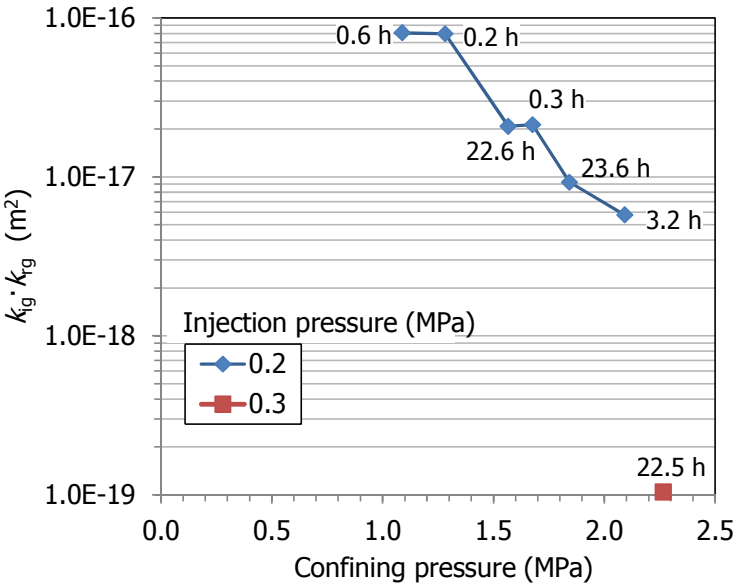

Fig. 19. Gas permeability measured in a sample from test CW2 including the interface between block and pellets. The duration of the steps is indicated in hours

4 Discussion

The tests presented allowed to follow the hydro-mechanical evolution of a two-component buffer material upon hydration under isochoric conditions at ambient temperature. The two components (bentonite pellets –GBM– and bentonite block) had different initial water contents and dry densities. Except in tests MGR27 and CW2, hydration took place through the pellets part, which had a higher intrinsic permeability than the block because of its lower dry density, higher macroporosity and

lower water content (Villar and Lloret 2001, Romero 2013). During the MGR tests the axial pressure was measured on the sample surface opposite to hydration.

The pressure development was not mainly related to the quantity of water taken (i.e. to the overall degree of saturation), but to the water intake rate. Thus, when hydration took place under very low water inflow rate (MGR22, MGR26), the axial pressure for a given overall degree of saturation was much higher than for the tests in which hydration took place more quickly (Fig. 4, right). Similarly, in test MGR27, in which hydration under constant injection pressure was slower because it took place through the higher-density block part, the pressure reached for a given overall degree of saturation was initially (namely until the overall degree of saturation reached ~60%) higher than for the tests in which saturation took place through the pellets. This suggests that it was the redistribution of water in the microstructure the mechanism that triggered most of the swelling. This is supported by the fact that in test MGR23 the axial pressure considerably increased during the 14-day period during which inadvertently no water was supplied to the cell, showing that water redistribution inside the bentonite can cause pressure increase. X-ray tomography scans of oedometer tests and image post-processing, allowed Massat et al. (2016) to correlate the evolution of swelling pressure and inter-aggregate porosity in compacted bentonite and conclude that water redistribution inside the structure led to reaching a stable swelling pressure. In the EB in situ test performed at the Mont Terri URL, where a large-scale two-component barrier (FEBEX GBM and blocks) was tested for 10.5 years, most of the sensors installed in the bentonite recorded relative humidity values of 100% only one year after the beginning of the test, whereas it took four years for the total pressure sensors to record stable values that kept approximately constant until the end of the test (García-Siñeriz et al. 2015).

The different strength of the materials involved also played a role on the axial pressure development kinetics at the first stages of saturation. When the water intake was very slow, the block part was able to swell relatively quickly (see the dry density and water content distribution at the end of test

MGR26 in Fig. 10), and because the pellet part was comparatively dry (drier than at the end of any other test) and consequently rigid, the stress was more effectively transmitted towards the top and hence recorded by the load cell. In contrast, when hydration was quicker, the pellet part soon collapsed and was easily compressed by the downwards swelling of the block, resulting in a lower axial load measured on top. In fact, a downwards movement of the pellets/block interface in cell CW1 was observed, indicating the compression (or collapse) of the pellets part. In contrast this interface moved upwards in cell CW2, saturated through the block.

The final axial pressure measured in the tests is plotted against the final degree of saturation in Fig. 20. Overall the pressure consistently increased with the average degree of saturation, but in test MGR26, saturated under low water inflow, a pressure higher than expected according to the trend marked by the other tests was reached, consistent with the description of the initial stages of saturation given in the previous paragraph. Once full saturation was reached the swelling pressure was the same irrespective of the way of saturation, and thus tests MGR22 and MGR23 showed the same final pressure (3 MPa). This value is higher than the swelling pressure expected for a FEBEX bentonite sample compacted to the average dry density value of the MGR tests (1.45 g/cm^3). The theoretical value would be 2.0±0.5 MPa, according to the empirical correlation between dry density and swelling pressure obtained in small standard oedometers (Eq. 3). Previous researches suggested that there is a scale effect on the swelling pressure measured in the laboratory, which tends to be higher as the testing cell is larger (Imbert & Villar 2006).

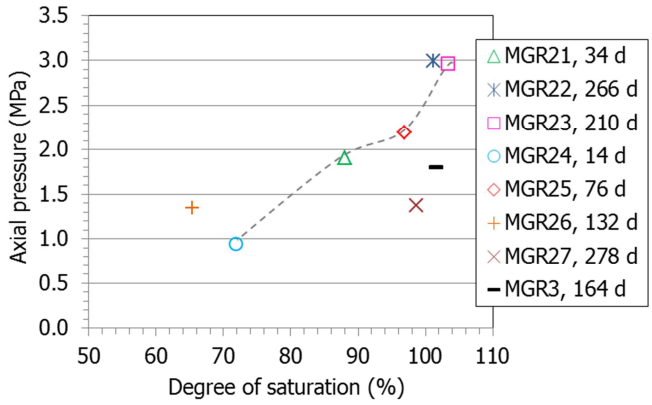

Fig. 20. Final axial pressures measured as a function of the final degree of saturation of MGR tests (average ρ_d=1.45 g/cm^3)

Even though full saturation had not been reached in test MGR27 (final S_r=99%), the final pressure measured in this test was much lower than could be expected according to the general trend for tests in which saturation took place through the pellets shown in Fig. 20. Hydration tests performed in large-scale cells where radial and axial pressures were measured at different heights along the sample length showed that during saturation, the transient pressure values were related to the local dry density (Dueck et al. 2016, Baryla et al. 2019, Bian et al. 2019, Bernachy-Barbe et al. 2020, Harrington et al. 2020). In the case of test MGR27, the pellets part, on top of the sample, had the final lowest dry density (Fig. 10) and lower degree of saturation (Fig. 21). It is likely that the axial load measured reflected mainly the local pressure at the upper part of the sample, which would be lower than the pressure that would have been measured at the bottom (in the block part) if there had been a pressure sensor in the area. In other words, the axial pressure measured on top would not be fully representative of the average pressure developed by the sample, because it would also be affected by the local conditions on top of the sample (lower density and degree of saturation). Similarly, the axial top pressure measured in the rest of the tests would also be conditioned by the higher dry densities in this area, where the block was placed (Fig. 10). Hence, in addition to the scale effect

commented in the previous paragraph, a further reason for the higher than expected pressures observed would be the influence of the higher density close to the measuring area on top.

As a further corroboration of that hypothesis, the final swelling pressure reached in a test performed in the same oedometer with a mixture of regular-shaped FEBEX bentonite pellets and powder in a 70/30 ratio has also been included in the Figure (test MGR3). The average dry density of this mixture was 1.45 g/cm^3 (as in the MGR tests presented here) and the initial water content 13.6% (Villar 1999). In this case the swelling pressure of the saturated sample had an intermediate value between the trend for tests having the pellets on top and the test with the block on top (MGR27). This would reflect the intermediate value of dry density on the top part of the sample, which was 1.43 g/cm^3 at the end of test MG3, 1.46 g/cm^3 at the end of tests MGR22 and MGR23 and 1.42 g/cm^3 at the end of test MGR27, which in addition was less saturated.

The tests performed by Martikainen et al. 2018 (reported in Talandier, 2019) were very similar in design and dimensions to the tests presented here, with hydration under an injection pressure of 10 kPa taking place through the pellets (hence comparable to tests MGR21, MGR23 to MGR25). Hydration took place through the top surface, where the pellets were placed. In these tests MX-80 bentonite was used and the radial pressure developed by the block and the pellets parts were measured in addition to the axial ones. The axial and radial pressure development in the areas farther away from hydration (i.e. around the block part) displayed the initial peak followed by a decrease and a smooth eventual increase observed in some MGR tests (Fig. 4). These measurements also showed significantly lower pressures in the pellets than in the block part. The modelling groups involved in a benchmark where these tests were analysed, concluded that this difference was due to the initial contrast of density between the top and bottom of the sample but also to the friction between the bentonite and the steel cell wall (Talandier, 2019).

Indeed none of the tests reached a final complete homogeneity in terms of dry density or water content: the water content decreased from the hydration surface upwards whereas the dry density increased (Fig. 10). These heterogeneities resulted from the initial swelling and resulting density decrease of the bentonite that became first saturated (those parts closest to the bottom hydration surface), and the consequent compression of the bentonite located upwards. In contrast, a final homogeneous degree of saturation close to 100% was reached in the longer tests saturated through the pellets, i.e. MGR22, MGR23 and CW1 (Fig. 21). Once overall full saturation was reached, no further water content or dry density changes are to be expected, which would mean that part of the initial volume changes were irreversible. Also in the large-scale EB test mentioned above, no spatial trends were found for the degree of saturation, despite the fact that density and water content gradients remained (García-Siñeriz et al. 2015). In all cases the pellets/block interface did not seem to have any effect on the continuous gradients observed, i.e. there were no sudden changes across the interface.

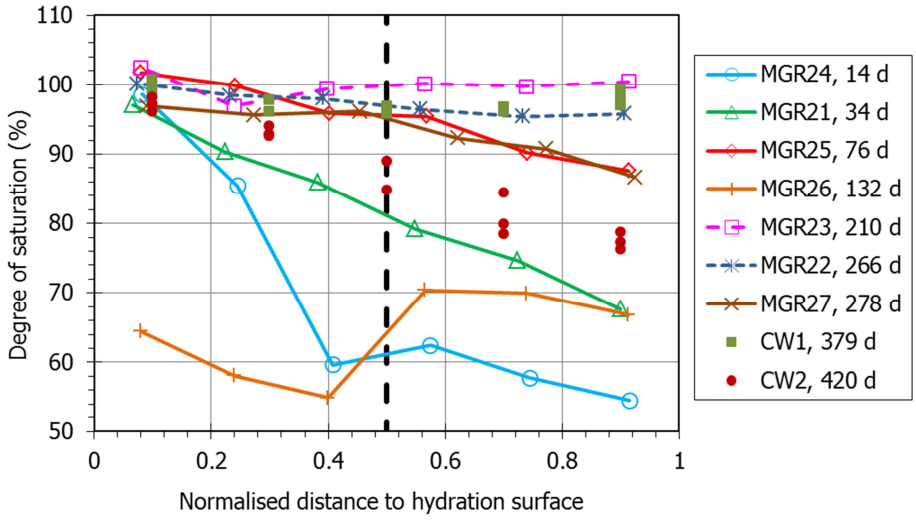

Fig. 21. Final degree of saturation along the samples of MGR and CW tests (total length of 10 cm in tests MGR and 12 cm in CW). Hydration took place through the pellets except in tests MGR27 and CW2. The duration of the tests is indicated in days

The two tests in which hydration took place through the block (MGR27 and CW2) were far from full saturation, despite the fact that they were the longest ones performed in each kind of cell. It is remarkable that in all the tests the area closest to the hydration surface was fully saturated, except in test MGR26. This test, performed under constant flow and lasting 132 days, did not follow the overall trend, since the increase in water content was moderate and similar for both halves, attesting the more homogeneous water redistribution allowed by slow hydration. Vapour diffusion in the pore spaces would be the water transfer mechanism away from the hydration surface, as postulated by Kröhn (2005), who described the time-dependent water content distribution during the saturation of compacted bentonite under laboratory conditions by Fick's second law. Eventually, when full saturation was reached, the differences in the physical state of samples saturated under constant pressure or flow obliterated, resulting in the similar water content and dry density distribution patterns of tests MGR22 and MGR23.

Concerning the microstructural modifications during hydration, the GBM and the block parts behaved quite differently and in fact most parameters inferred by MIP (volume and size of each pore range, ratio between them), were different for the two components of the samples. Unlike the physical variables discussed in the previous paragraphs, in most tests there was not a smooth change between the microstructural parameters of pellets and block. The most notable change in the pellets parts was the disappearance of the pores larger than 550 μm and the overall drastic decrease in size and volume of macropores. In contrast, the mean size of the pores smaller than 200 nm increased with respect to the original values for all the pellets subsamples. This was also the case for the block samples. Furthermore, in the block subsamples the volume and size of the macropores tended to increase, except in the shorter, less saturated tests. The increase of both e_m and e_M in the blocks subsamples resulted from the overall decrease in dry density experienced by the block upon hydration. Nevertheless, the e_m/e_M ratio increased from the initial ~0.3 to values higher than 0.7 in all samples, but much more significantly in the pellets samples. Only the driest pellets samples

(corresponding to the shorter tests, test MGR26 performed under constant flow, and test CW2 saturated through the block) had e_m/e_M ratios close to the initial one. These samples kept also pores larger than 550 μm that cannot be detected by MIP (because of the technique limitations) but were inferred as explained at the beginning of section 3.3. Pores larger than ~70 μm were actually observed by MIP in some pellets samples of test CW2 (Fig. 16), where the pellets part was not completely saturated. Closing of large voids (or very low density areas filled by powder) between regular-shaped bentonite pellets upon hydration was observed by X-ray computed tomography by van Geet et al. (2005), Molinero et al. (2018) and Reijonen et al. (2020), among others.

The only sample that kept quite homogeneous values across the pellets/block interface, in terms of e_m, e_M and mean pore sizes, was that from test MGR27. This was also the test reaching a highest homogeneity concerning dry density and water content, which suggests that the microstructural changes were related to the changes in dry density and water content and thus to temporal evolution.

Hence, as a result of hydration the volume of micropores increased in all the bentonite with respect to the initial one, particularly in the case of the pellets. The increase in the volume of micropores was likely related to the increase in the smectite basal spacing as a result of the hydration of the interlayer cations (Fig. 18), which is the driving mechanism for crystalline swelling, predominant in compacted bentonite saturated under isochoric conditions (e.g. Pusch et al. 1990, Devineau et al. 2006). Holmboe et al. (2012) determined by XRD profile fitting that in bentonite samples saturated under confined conditions the interlayer porosity dominated total porosity and for dry densities 1.4-1.8 g/cm^3 the interparticle porosity was ≤3%. As it happened with the pore size distribution obtained by MIP, the basal spacings were clearly distinct for pellets and block samples. In contrast, the basal spacings determined in wet samples from the in situ EB experiments (using the same procedure and methodology as in this work) did not show clear differences between block and pellets (Villar et al. 2014). Since the samples from the in situ test were matured for 10.5 years, it could be expected that

in the long term, also the microstructure of the two components of the much shorter MGR tests would become homogenised. In samples from the in situ test –which were fully saturated– the basal spacings indicated that 3 water layers were completely developed in the interlayer (values around 1.85 nm). For water contents below ~38%, the basal spacing increased with the water content, but for higher values the basal spacing was quite constant, irrespective of the water content, which was also observed in the samples from the MGR tests.

5 Conclusions

The hydro-mechanical evolution of a two-component bentonite buffer material –low density pellets mixtures and higher density compacted blocks– was studied by means of a series of laboratory hydration tests performed under isochoric conditions. The tests were performed in a large-scale oedometer (10x10 cm) and in a transparent cell (12x12x2 cm). In the first case the axial pressure was measured on the sample surface opposite to hydration. In most tests hydration took place through the pellets part, but the effect of hydrating through the block was also checked. As well, tests were performed either under a low water injection pressure or under a low water inflow rate.

The analysis of the results obtained allowed to draw the following conclusions:

- Because of their low density and large macroporosity, hydration through the pellets was initially quick, even though the water injection pressure was very low.
- The way of hydration conditioned the water intake and the pressure development kinetics. Slow hydration (e.g. under a controlled low flow of through the block) delayed the start of pressure development, but allowed higher pressures to be reached for lower overall degrees of saturation. The reason could be the longer time available for water redistribution from the macropores to the microstructure (particularly the montmorillonite interlayer), which would be the responsible for swelling. The interplay between the different strengths of the two

components may also be a relevant factor on the axial load measured at the first stages of saturation.

- Irrespective of the way of saturation (constant flow or pressure), the pressure development was not continuous. After a first sharp increase (which was quicker under constant pressure), there was an intermediate period of pressure stabilisation. Only when the overall degree of saturation was very high, the pressure increased again until its final equilibrium value. This pressure development pattern had been previously observed also in samples of compacted bentonite and of pellets.
- The stress measuring devices (in this case an external load cell on top of the oedometer cover) reflect local stresses which are conditioned by the local dry density. Hence, when the block part was on top, the final pressure value of the saturated sample was higher than the value expected for smaller samples of bentonite compacted at the same average dry density. When the pellet part was on top, the contrary happened. Friction between the bentonite and the cell steel wall could also contribute to these differences. This research has put forward the necessity of using testing devices in which pressure can be measured at different locations to correctly assess the stress state of inhomogeneous samples.
- Bentonite water content and dry density gradients were observed at the end of the tests. For a given hydration rate they were dependent on the hydration time and, although they attenuated over time, they persisted even after full saturation was reached. Saturation under very low water inflow rate (either imposed or resulting from the low permeability of the block part when saturation took place through it) resulted in more uniform water contents and smoother gradients, also in terms of pore sizes.
- In contrast, the microstructure of the bentonite in the two components was very different even after full saturation. Despite of the drastic reduction in the volume and size of macropores in the pellets parts, they continued to be higher than in the block part and consequently the e_m/e_M was

lower in the pellets part. The basal spacing of the smectite, which is an indication of the number of water layers in the interlayer, was higher in pellets samples than in block samples. However, an overall trend to pore size homogenisation towards smaller sizes over time was observed.

– The water content and dry density gradients were not affected by the pellets/block interface. After full saturation the pellets/block interface was impervious to gas.

The behaviour of a two-component barrier can be affected by the particular dry density and water content of each barrier component as well as their size and geometry, and by the boundary conditions, such as the existence of gaps, temperature and water salinity and availability. This research has just analysed the effect of geometry and water availability, but there are not systematic published researches having analysed all the other aspects yet.

The evidence provided by these experimental results along with the outcomes of the large-scale EB test, in which a similar two-component barrier was tested for 10.5 years, suggests that, although the initial heterogeneity of the barrier system and the deformations induced in the first stages of saturation tend to attenuate over time, residual inhomogeneities will persist and remain even after full saturation. The kind and extent of these heterogeneities will depend on the initial and boundary conditions of the barrier.

Acknowledgements

The research leading to these results was financed by the Beacon project, which receives funding from the Euratom Research and Training Programme 2014–2018 under grant agreement number 745942. Part of the laboratory work was carried out by J. Aroz. Dr. Pedro Luis Martín of CIEMAT contributed to the design of the tests in transparent cell. The mercury intrusion porosimetry tests were performed at the Petrophysical laboratory of CIEMAT by N. Brea. The XRD measurements were performed at the High-Level Radioactive Waste Unit of CIEMAT and at the Unidad de Técnicas

Geológicas del CAI de Ciencias de la Tierra y Arqueometría of the Universidad Complutense de Madrid. L. Gutiérrez-Nebot (CIEMAT) performed the XRD interpretation. Beatriz Carbonell was hired in the framework of the Spanish National System of Youth Guarantee in R+D 2014, with financing of the European Social Fund and the Youth Employment Initiative.

CRediT statements

M.V. Villar: conceptualization, formal analysis, investigation, writing, editing, supervision

R.J. Iglesias: investigation, formal analysis, resources, visualization, review

C. Gutiérrez-Álvarez: investigation, formal analysis, resources, visualization, review

B. Carbonell: investigation, formal analysis, resources, visualization, review

6 References

Abed, A., Solowski, W.T. 2019. Simulation of swelling pressure evolution during infiltration in a bentonite block-pellet laboratory scale test. Japanese Geotechnical Society Special Publication 7(2): 323-330. DOI: 10.3208/jgssp.v07.052

Alcantara A, Romero E., Mokni N., Olivella S. 2020. Microstructural and hydro-mechanical behaviour of bentonite pellets and powder mixtures. E-UNSAT 2020. E3S Web of Conferences 195, 04003. https://doi.org/10.1051/e3sconf/202019504003

Baryla, P., Bernachy-Barbe, F., Bosch, J.A., Campos, G., Carbonell, B., Daniels, K.A., Ferrari, A., Guillot, W., Gutiérrez-Álvarez, C., Harrington, J.F., Iglesias, R.J., Kataja, M., Mašín, D., Najser, J., Rinderknecht, F., Schäfer, T., Sun, H., Tanttu, J., Villar, M.V., Wieczorek, K. 2019. Bentonite

mechanical evolution – experimental work for the support of model development and validation. DELIVERABLE (D4.1/2). Report. 132 pp.

Bernachy-Barbe, F., Conil, N., Guillot, W., Talandier, J. 2020. Observed heterogeneities after hydration of MX-80 bentonite under pellet/powder form. Applied Clay Sience 189: 105542. https://doi.org/10.1016/j.clay.2020.105542

Bernachy-Barbe, F. 2021. Homogenization of bentonite upon saturation: Density and pressure fields. Applied Clay Sience 209: 106122. https://doi.org/10.1016/j.clay.2021.106122

Bian, X., Cui, Y.J., Zeng, L.L., Li, X.Z. 2019. Swelling behavior of compacted bentonite with the presence of rock fracture. Engineering Geology 254: 25-33. https://doi.org/10.1016/j.enggeo.2019.04.004

Bosgiraud, J.M., Foin, R. 2016. Test report on FSS metric clayish material emplacement tests with clayish material definition and laboratory work on its performance. Project DOPAS Work Package 3 - Deliverable 3.7. European Commission Grant Agreement No. 323273. 35 pp. https://igdtp.eu/documents/

Devineau, K., Bihannic, I., Michot, L., Villiéras, F., Masrouri, F., Cuisinier, O., Fragneto, G., Michau, N., 2006. In situ neutron diffraction analysis of the influence of geometric confinement of crystalline swelling of montmorillonite. Applied Clay Science 31 (1–2): 76–84. https://doi.org/10.1016/j.clay.2005.08.006

Dixon, D., Chandler, N., Graham, J., Gray, M.N., 2002. Two large-scale sealing tests conducted at atomic energy of Canada's underground research laboratory: the buffer-container experiment and the isothermal test. Canadian Geotechnical Journal 39: 503–518. https://doi.org/10.1139/t02-012

Dueck, A., Goudarzi, R., Börgesson, L. 2016. Buffer homogenisation. Status report 3. Technical Report SKB TR-16-04. Svensk Kärnbränslehantering, Stockholm, 104 pp.

ENRESA 2005. Engineered barrier emplacement experiment in Opalinus Clay for the disposal of radioactive waste in underground repositories. Final Report. Publicación Técnica ENRESA 02/05. Madrid, 101 pp.

ENRESA 2006. FEBEX Full-scale Engineered Barriers Experiment, Updated Final Report 1994–2004. Publicación Técnica ENRESA 05-0/2006, Madrid, 590 pp.

Gaus, I., Garitte, B., Senger, R., Gens, A., Vasconcelos, R., García-Sineriz, J.L., Trick, T., Wieczorek, K., Czaikowski, O., Schuster, K., Mayor, J.C., Velasco, M., Kuhlmann, U., Villar, M.V. 2014. The HE-E Experiment: Lay-out, Interpretation and THM Modelling. Nagra Arbeitsbericht NAB 14-53. Wettingen, 140 pp.

Gens, A., Alcoverro, J., Blaheta, R., Hasal, M., Michalec, Z., Takayama, Y., Lee, C., Lee, J., Kim, G.Y., Kuo, W.J., Lin, C.Y. 2021. HM and THM interactions in bentonite engineered barriers for nuclear waste disposal. International Journal of Rock Mechanics and Mining Sciences 137: 104572. https://doi.org/10.1016/j.ijrmms.2020.104572

Gutiérrez-Rodrigo, V. 2018. Transporte de gas en materiales de barrera. Tesis Doctoral. Universidad Complutense de Madrid. Colección Documentos CIEMAT. ISBN: 978-84-7834-802-2. Madrid, 303 pp.

Gutiérrez-Rodrigo, V., Martín, P.L., Villar, M.V. 2021. Effect of interfaces on gas breaktrough pressure in compacted bentonite used as engineered barrier for radioactive waste disposal. Process Safety and Environmental Protection 149: 244-257. https://doi.org/10.1016/j.psep.2020.10.053.

Grambow, B. 2016. Geological disposal of radioactive waste in clay. Elements 12: 239-245. DOI: 10.2113/gselements.12.4.239

Harrington, J.F., Daniels, K.A., Wiseall, A.C., Sellin, P., 2020. Bentonite homogenisation within engineered cavities: the evolution of swelling pressure during bentonite hydration. International Journal of Rock Mechanics and Mining Sciences 136, 104535. doi:10.1016/j.ijrmms.2020.104535.

Hoffmann, C. 2005. Caracterización hidromecánica de mezclas de pellets de bentonita. Estudio experimental y constitutivo. (PhD Thesis), Universitat Politècnica de Catalunya, Barcelona, 387 pp.

Hoffmann, C., Alonso, E.E. and Romero, E. 2007. Hydro-mechanical behaviour of bentonite pellet mixtures. Physics and Chemistry of the Earth 32: 832-849. https://doi.org/10.1016/j.pce.2006.04.037

Holmboe, M., Wold, S., Jonsson, M. 2012. Porosity investigation of compacted bentonite using XRD profile modeling. Journal of Contaminant Hydrology 128: 19-32. doi:10.1016/j.jconhyd.2011.10.005

Imbert, C., Villar, M.V. 2006. Hydro-mechanical response of a bentonite pellets/powder mixture upon infiltration. Applied Clay Science 32: 197-209. https://doi.org/10.1016/j.clay.2006.01.005

Imbert, C., Gatabin, C., Maugis, P., Leboulch, D., Mouche, E. 2002. Hydro-mechanical behaviour of a heterogeneous swelling clay material. In: Auriault, J.L., Block, J.F., Geindreau, C., Royer, P. Bloch, J.F., Boutin, C., Lewandowska, J. (Eds.) Poromechanics II: Proceedings of the Second Biot Conference on Poromechanics, Grenoble. Swets & Zeitlinger, Balkema, Lisse. 225-230.

Kennedy, K., Verfuss, F., Plötze, M. 2004. Engineered Barrier Emplacement (EB) Experiment in Opalinus Clay: Granular material backfill product documentation. EC contract FIKW-CT-2000-00017. Project Deliverable D3c. Mont Terri Technical Note 2004-17, 61 pp.

Kröhn, K.P. 2005. New evidence for the dominance of vapour diffusion during the re-saturation of compacted bentonite. Engineering Geology 82: 127-132. https://doi.org/10.1016/j.enggeo.2005.09.015

Lloret A., Villar M.V., Sánchez M., Gens A., Pintado X., Alonso E.E. 2003. Mechanical behaviour of heavily compacted bentonite under high suction changes. Géotechnique 53 (1): 27-40. https://doi.org/10.1680/geot.53.1.27.37258

Martikainen, J., Pintado, X., Mamunul, H. 2018. Laboratory tests to evaluate bentonite homogenization. Internal memorandum POS-026579. Eurajoki, Finland: Posiva Oy.

Mašín, D. 2013. Double structure hydromechanical coupling formalism and a model for unsaturated expansive clays. Engineering Geology 165: 73-88. https://doi.org/10.1016/j.enggeo.2013.05.026

Massat, L., Cuisinier, O., Bihannic, I., Claret, F., Pelletier, M., Masrouri, F., Gaboreau, S. 2016. Swelling pressure development and inter-aggregate porosity evolution upon hydration of a compacted swelling clay. Applied Clay Science 124–125: 197-210. https://doi.org/10.1016/j.clay.2016.01.002

Molinero Guerra, A. 2018. Caractérisations expérimentale et numérique du comportement hydro-mécanique d'un matériau hétérogène : mélange de poudre/pellets de bentonite. Ph. Thesis, Université Paris-Est. 190 pp.

Molinero Guerra, A., Cui, Y.-J., Mokni, N., Delage, P., Bornert, M., Aimedieu, P., Tang, A.M., Bernier F. 2018. Investigation of the hydro-mechanical behaviour of a pellet/powder MX80 bentonite

mixture using an infiltration column. Engineering Geology 243: 18-25. 10.1016/j.enggeo.2018.06.006

Müller, H.R., Garitte, B., Vogt, T., Köhler, S., Sakaki, T., Weber, H., Spillmann, T., Hertrich, M., Becker, J.K., Giroud, N., Veerle, C., Diomidis, N. Vietor, T. 2017. Implementation of the full-scale emplacement (FE) experiment at the Mont Terri rock laboratory. Swiss Journal of Geosciences 110: 287–306. DOI 10.1007/s00015-016-0251-2

NAGRA 2019. Implementation of the Full-scale Emplacement Experiment at Mont Terri: Design, Construction and Preliminary Results. NAGRA Technical Report NTB 15-02. Wettingen, 147 pp.

Navarro, V., Asensio, L., Morena, G. de la, Gharbieh, H., Alonso, J., Pulkkanen, V.M. 2020. From double to triple porosity modelling of bentonite pellet mixtures. Engineering Geology 274: 105714. https://doi.org/10.1016/j.enggeo.2020.105714

Pusch, R., Karnland, O., Hökmark, H. 1990. GMM -A general microstructural model for qualitative and quantitative studies on smectite clays. SKB Technical Report TR 90-43. Stockholm, 94 pp.

Reijonen, H.M., Kuva, J., Heikkilä, P. 2020. Benefits of applying X-ray computed tomography in bentonite based material research focussed on geological disposal of radioactive waste. Environmental Science and Pollution Research 27: 38407–38421. https://doi.org/10.1007/s11356-020-08151-2

Romero, E. 2013. A microstructural insight into compacted clayey soils and their hydraulic properties. Eng. Geol. 165: 3-19. http://dx.doi.org/10.1016/j.enggeo.2013.05.024

Salo, J.P., Kukkola, T. 1989. Bentonite pellets, an alternative buffer material for spent fuel canister deposition holes. Workshop “Sealing of Radioactive Waste Repositories”. Braunschweig.

Sánchez M, Gens A, Guimarães L, Olivella, S, 2005. A double structure generalized plasticity model for expansive materials. International Journal for Numerical and Analytical Methods in Geomechanics 29: 751–787. DOI:10.1002/nag.434.

Sellin, P., Leupin, O., 2013. The use of clays as an engineered barrier in radioactive-waste management – a review. Clays and Clay Minerals 61 (6): 477–498. https://doi.org/10.1346/CCMN.2013.0610601

Sing, K.S.W., Everett, D.H., Haul, R.A.W., Moscou, L., Pierotti, R.A., Rouquérol, J., Siemieniewska, T. 1985. Reporting physisorption data for gas/solid systems with special reference to the determination of surface area and porosity. Pure and Applied Chemistry 57(4): 603-619. IUPAC.

SKB. 2010. Buffer, Backfill and Closure Process Report for the Safety Assessment SR-Site. TR-10-47. Swedish Nuclear Fuel and Waste Management Co (SKB), Stockholm, 360 pp.

Talandier, J. (Ed.) 2019. Synthesis of results from task 5.1. BEACON Deliverable D5.1.2. 334 pp.

Van Geet, M., Volckaert, G., Roels, S. 2005. The use of microfocus X-ray computed tomography in characterising the hydration of a clay pellet/powder mixture. Applied Clay Science 29 (2): 73-87. https://doi.org/10.1016/j.clay.2004.12.007

Van Geet, M., Bastiaens, W., Volckaert, G., Weetjens, E., Sillen, X., Maes, N., Imbert, C., Billaud, P., Touzé, G., Filippi, M., Plas, F., Villar, M. V., García-Gutiérrez, M., Mingarro, M., Gens, A., Vallejan, B. 2009. RESEAL II. A large-scale in situ demonstration test for repository sealing in an argillaceous host rock - Phase II. Final report.: EUR 24161, Nuclear Science and Technology, European Commission, Luxembourg, 288 pp.

Villar, M.V. 1999. RESEAL Project. Topical Report on Laboratory Tests. Version 1. Informe Técnico CIEMAT/DIAE/54121/2/99. Madrid, 33 pp.

Villar, M.V. 2002. Thermo-hydro-mechanical characterisation of a bentonite from Cabo de Gata. A study applied to the use of bentonite as sealing material in high level radioactive waste repositories. Publicación Técnica ENRESA 01/2002, Madrid, 258 pp.

Villar, M.V. 2012. EB experiment. Laboratory infiltration tests report. PEBS Deliverable D2.1-5. CIEMAT Technical Report CIEMAT/DMA/2G210/03/2012. 33 pp. https://www.pebs-eu.de/PEBS/EN/Downloads/D2_1_5_pdf.pdf?__blob=publicationFile&v=1

Villar, M.V.(Ed). 2017. FEBEX-DP Postmortem THM/THC Analysis Report. NAB 16-017. 143 pp.

Villar, M.V., Lloret, A. 2001. Variation of the intrinsic permeability of expansive clays upon saturation. In: Adachi, K., Fukue, M. (Eds.): Clay Science for Engineering. A.A. Balkema, Rotterdam, pp. 259–266.

Villar, M.V., Gómez-Espina, R. 2012. Long-term Performance of Engineered Barrier Systems PEBS. Permeability tests in samples from the EB experiment at Mont Terri (Borehole EB-B1). Technical Note CIEMAT/DMA/2G210/06/12. Madrid, 15 pp.

Villar, M.V.; Gutiérrez-Rodrigo, V.; Martín, P.L.; Romero, F.J. & Barcala, J.M. 2013. Gas transport in bentonite. Informes Técnicos CIEMAT 1301. Madrid, 63 pp. DOI: 10.13140/RG.2.2.14334.28489

Villar, M.V., Campos, R., Gutiérrez-Nebot, L. 2014. EB experiment. Laboratory post-mortem analyses report. PEBS Project Deliverable D2.1-7. CIEMAT Technical Report CIEMAT/DMA/2G210/01/2014. Madrid, 34 pp.

Villar, M.V., Iglesias, R.J., Gutiérrez-Álvarez, C., Carbonell, B., Campos, R., Campos, G., Martín, P.L., Castro, B. 2018. FEBEX-DP: Thermo-hydro-mechanical postmortem analysis of bentonite performed at CIEMAT. Technical report CIEMAT/DMA/2G216/2/16. NAB16-024. Madrid, 134 pp.

Villar, M.V., Campos, G., Gutiérrez-Nebot, L., Arroyo, X. 2019. Effect of prolonged drying at high temperature on the water retention capacity of bentonite (FEBEX-DP samples). Applied Clay Science 182: 105290. https://doi.org/10.1016/j.clay.2019.105290

Villar, M.V., Iglesias, R.J., García-Siñeriz, J.L., Lloret, A., Huertas, F. 2020. Physical evolution of a bentonite buffer during 18 years of heating and hydration. Engineering Geology 264: 105408. https://doi.org/10.1016/j.enggeo.2019.105408

Villar, M.V., Carbonell, B., Martín, P.L., Gutiérrez-Álvarez, C. 2021. The role of interfaces in the bentonite barrier of a nuclear waste repository on gas transport. Engineering Geology 286: 106087. https://doi.org/10.1016/j.enggeo.2021.106087

Volckaert, G., Bernier, F., Alonso, E., Gens, A., Samper, J., Villar, M.V., Martín, P.L., Cuevas, J., Campos, R., Thomas, H.R., Imbert, C., Zingarelli, V. 1996. Thermal-hydraulic-mechanical and geochemical behaviour of the clay barrier in radioactive waste repositories (model development and validation). Nuclear science and technology. EUR 16744. Commission of the European Communities, Luxembourg, 722 pp.

Volckaert, G., Dereeper, B., Put, M., Ortiz, L., Gens, A., Vaunat, J., Villar, M.V., Martín, P.L., Imbert, C., Lassabatère, T., Mouche, E., Cany, F. 2000. A large-scale in situ demonstration test for repository sealing in an argillaceous host rock. Reseal project – Phase I. EUR 19612. Commission of the European Communities, Luxembourg, 273 pp.

Yuan, S., Liu, X., Romero, E., Delage, P., Buzzi, O. 2020. Discussion on the separation of macropores and micropores in a compacted expansive clay. Géotechnique Letters 10: 1–7. https://doi.org/10.1680/jgele.20.00056